MAGIC matrices: freeform bioprinting materials to support complex and reproducible organoid morphogenesis

Austin J. Graham[1,2], Michelle W.L. Khoo[2], Vasudha Srivastava[1], Sara Viragova[3], Honesty Kim[1,2], Kavita Parekh[4], Kelsey M. Hennick[5], Malia Bird[1], Nadine Goldhammer[6], Jie Zeng Yu[6], Cameron D. Morley[4], Paul Lebel[2], Sanjay Kumar[4,7,8], Jennifer M. Rosenbluth[2,6], Tomasz J. Nowakowski[5], Ophir Klein[3,9], Rafael Gómez-Sjöberg[2,*], Zev J. Gartner[1,2,8,10,*]

[1]Department of Pharmaceutical Chemistry, University of California San Francisco, San Francisco, CA
[2]Chan Zuckerberg Biohub SF, San Francisco, CA
[3]Department of Orofacial Sciences, University of California San Francisco, San Francisco, CA
[4]Department of Bioengineering, University of California Berkeley, Berkeley, CA
[5]Weill Institute for Neurosciences, University of California San Francisco, San Francisco, CA
[6]Department of Medicine, University of California San Francisco, San Francisco, CA
[7]Department of Chemical and Biomolecular Engineering, University of California Berkeley, Berkeley, CA
[8]Department of Bioengineering and Therapeutic Sciences, University of California San Francisco, San Francisco, CA
[9]Department of Pediatrics, Cedars-Sinai Guerin Children's, Los Angeles, CA
[10]Center for Cellular Construction, University of California San Francisco, San Francisco, CA
*Correspondence: zev.gartner@ucsf.edu and rafael.gomez@czbiohub.org

Abstract:

Organoids are powerful models of tissue physiology, yet their applications remain limited due to their relatively simple morphology and high organoid-to-organoid structural variability. To address these limitations we developed a soft, composite yield-stress extracellular matrix that supports optimal organoid morphogenesis following freeform 3D bioprinting of cell slurries at tissue-like densities. The material is designed with two temperature regimes: at 4 ˚C it exhibits reversible yield-stress behavior to support long printing times without compromising cell viability. When transferred to cell culture at 37 ˚C, the material cross-links and exhibits similar viscoelasticity and plasticity to basement membrane extracts such as Matrigel. We first characterize the rheological properties of MAGIC matrices that optimize organoid morphogenesis, including low stiffness and high stress relaxation. Next, we combine this material with a custom piezoelectric printhead that allows more reproducible and robust self-organization from uniform and spatially organized tissue "seeds." We apply MAGIC matrix bioprinting for high-throughput generation of intestinal, mammary, vascular, salivary gland, and brain organoid arrays that are structurally similar to those grown in pure Matrigel, but exhibit dramatically improved homogeneity in organoid size, shape, maturation time, and efficiency of morphogenesis. The flexibility of this method and material enabled fabrication of fully 3D microphysiological systems, including perfusable organoid tubes that experience cyclic 3D strain in response to pressurization. Furthermore, the reproducibility of organoid structure increased the statistical power of a drug response assay by up to 8 orders-of-magnitude for a given number of comparisons. Combined, these advances lay the foundation for the efficient fabrication of complex tissue morphologies by canalizing their self-organization in both space and time.

Introduction

In vitro tissue models that reproducibly and scalably recapitulate complex tissue physiology are required for applications in regenerative medicine, disease modeling, and drug testing[1–8]. Organoids have the potential to satisfy these requirements. Organoids are self-organizing tissues derived from stem and progenitor cells that incorporate multiple mature cell types and simple morphological features. In order to self-organize, organoids must be derived from the appropriate cellular progenitors and cultured within the appropriate 3D microenvironments, typically laminin-rich extracellular matrix (ECM) gels like Matrigel[9–14]. Even when these requirements are satisfied, however, organoids lack developmental and anatomical contexts that support, constrain, and guide their morphogenesis in vivo. Consequently, they lack much of the complex morphology of the tissue from which they are derived and generally suffer from a high degree of structural heterogeneity[15–21]. Though some of this heterogeneity is intrinsic to the stochastic nature of cell and tissue growth and morphogenesis, there are significant external factors such as initial tissue size, composition, media access, and neighboring interfaces that contribute to morphological heterogeneity[22]. These manifest as differences in organoid mass, structural features, and cellular composition, all of which lead to variability in the response to drug, microenvironmental, or genetic perturbations (Fig. 1A). This variability in turn decreases statistical precision between experimental conditions, requiring many replicates to elucidate phenotypes.

To address these challenges, engineering platforms have sought to better control the initial conditions from which organoids emerge. Such platforms include microwell arrays, microphysiological systems (or organs-on-a-chip), and 3D bioprinting. Microwell arrays are screening platforms that emerge from high-density cell aggregates, generally of a composition defined by Poisson statistics, and arranged spatially for straightforward imaging[23–25]. Microwells can improve organoid homogeneity but are generally limited in the eventual size and geometry of the resulting tissue. In microphysiologcial systems, controlled geometries are lithographically patterned on polymeric chips, which are then coated with cells and ECM to generate the microtissue[26–29]. These powerful tools allow for complex tissue geometries, incorporation of multiple cell types, and microfluidic plumbing for exchange of metabolites between tissue and organ compartments. However, the pre-defined geometry and artificial interfaces such as PDMS impose many constraints on the tissue that may impact normal morphogenesis. Additionally, the top-down constraints on geometry imposed by the workflow can incorporate biases on cell and tissue function. Finally, the chip format requires complete reconfiguration for each build iteration, slowing the design-build-test cycle. In contrast, 3D bioprinting comprises a suite of rapid prototyping tools that provides a potentially more flexible platform for generating tissues of defined size, composition, and geometry on-demand and in arbitrary microenvironments[30–38]. However, most applications of bioprinting remain in their infancy and have typically focused on printing non-living biomaterials or composites of hydrogels and cells. Moreover, these efforts mostly focus on controlling the printed geometry of cells and materials in 3D space, rather than the critical importance of the subsequent morphogenesis of these living materials in time. Consequently, little emphasis has been placed on the interaction between printed structures and the spatial, mechanical, and molecular details of the microenvironment that support their morphogenesis[39].

Recently, several applications of printing and patterning technology have attempted to better program cell and organoid morphogenesis by fabricating tissues from cell slurries at tissue-like densities, then embedding these seeds directly into gold-standard ECMs like Matrigel[40–44]. For example, DNA-programmed assembly of cells (DPAC) is a bottom-up method for patterning dense cell slurries in Matrigel and Matrigel-Collagen-I mixtures that has been applied to fibroblast clusters, mammary organoids, and vasculature[45–47]. Cells are first directed to self-assemble on a 2D template and then released into Matrigel as it polymerizes. They can then undergo morphogenesis in 3D. While this method is among the highest in resolution (on the order of a single cell) for printing microtissues, it lacks scalability, has limited height resolution, and can be technically arduous. Embedded bioprinting methods such as bioprinting-assisted tissue emergence (BATE) extrude dense cell slurries directly into liquid Matrigel or collagen to construct large 3D patterns that undergo morphogenesis[48]. These methods potentially address many of the scalability issues presented by DPAC. However, BATE remains limited by Matrigel's steep transition from fluid to solid as a function of temperature, which provides only a very narrow time window in which extruded cell slurries conform to the geometry prescribed by the printer. Consequently, the capacity of BATE to support automation and extended printing times has not been explored.

To extend available print times, freeform bioprinting has largely turned to granular media such as Carbopol or gelatin microgel slurries which provide improved bioprinting mechanics[49,50]. One central property of these materials is reversible yield-stress behavior, in which the slurry yields in response to the printhead entering the bath and extruding material, then recovers to provide elastic support to the extruded bioink once the nozzle is removed. However, most of these materials are not optimal for long-term cell growth and morphogenesis[51,52]. Several groups have introduced interstitial matrices derived from natural ECM like collagen I with the goal of improving cell survival and dynamics[53,54]. However, the mechanics and composition of the resulting materials elicit cell behaviors that can be challenging to predict. For example, collagen I-containing ECM strain-stiffens and is not optimized to support epithelial growth and morphogenesis compared to basement membrane extracts[48,55–58]. Matrigel in particular has several properties that make it unique as a biomaterial for tissue morphogenesis, but poor as a biomaterial for freeform bioprinting. It is rich in laminin, collagen IV and nidogen—the major components of the basement membrane that provide critical polarity signals to tissue supporting their early morphogenesis. Matrigel is also degradable, undergoes plastic deformations at long times scales, and is a viscoelastic biomaterial with a storage modulus significantly lower than typical synthetic materials used in 3D cell culture and bioprinting applications[59–61]. However, it is a poor support for embedded bioprinting because it behaves as a viscous fluid at 4 °C (Supplementary Movie 1), while quickly transitioning to a soft hydrogel at 37 °C for cell culture. Therefore, a freeform bioprinting material that combines the advantageous

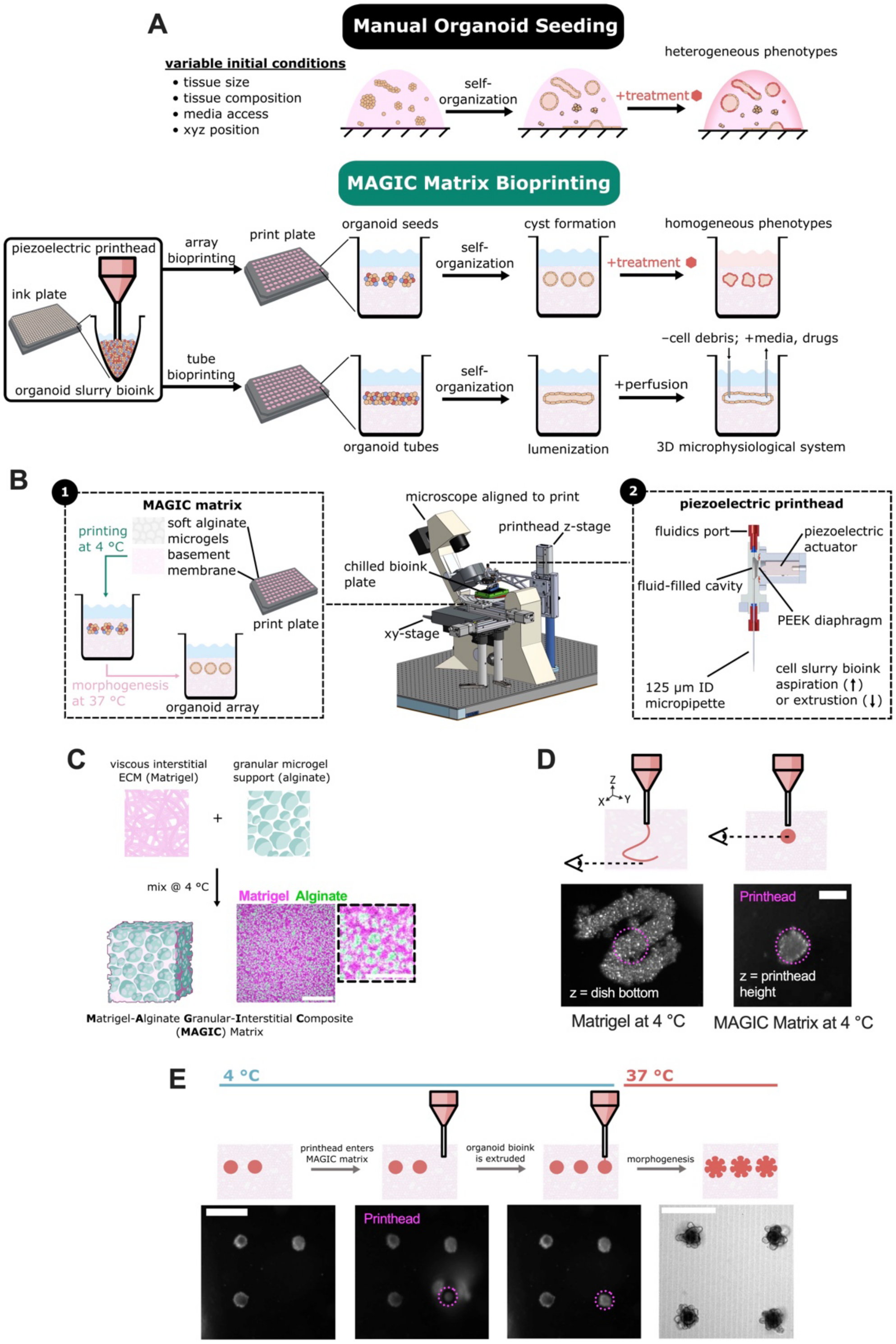
A
Manual Organoid Seeding
variable initial conditions
• tissue size
• tissue composition
• media access
• xyz position
self-organization
+treatment
heterogeneous phenotypes
MAGIC Matrix Bioprinting
piezoelectric printhead
ink plate
organoid slurry bioink
array bioprinting
tube bioprinting
print plate
organoid seeds
self-organization
cyst formation
+treatment
homogeneous phenotypes
organoid tubes
lumenization
+perfusion
−cell debris; +media, drugs
3D microphysiological system
B
1
MAGIC matrix
printing at 4 °C
soft alginate microgels
basement membrane
print plate
morphogenesis at 37 °C
organoid array
microscope aligned to print
printhead z-stage
chilled bioink plate
xy-stage
2
piezoelectric printhead
fluidics port
piezoelectric actuator
fluid-filled cavity
PEEK diaphragm
125 μm ID micropipette
cell slurry bioink aspiration (↑) or extrusion (↓)
C
viscous interstitial ECM (Matrigel)
granular microgel support (alginate)
+
mix @ 4 °C
Matrigel Alginate
Matrigel-Alginate Granular-Interstitial Composite (MAGIC) Matrix
D
Z
X
Y
Printhead
z = dish bottom
z = printhead height
Matrigel at 4 °C
MAGIC Matrix at 4 °C
E
4 °C
37 °C
printhead enters MAGIC matrix
organoid bioink is extruded
morphogenesis
Printhead

Figure 1. MAGIC extracellular matrices are embedded bioprinting materials that enable construction of uniform and complex organoid architectures. A. Traditional manual methods of seeding organoids lead to heterogeneity in organoid growth and morphogenesis due to heterogeneity in starting tissue size, composition, and microenvironment. By controlling for initial conditions such as cell number, media access, and organoid spacing, bioprinting platforms facilitate rapid generation of reproducible organoid arrays or freeform 3D microphysiological systems. **B.** MAGIC matrix bioprinting combines two major advances: (1) a soft embedded bioprinting material that supports gold-standard morphogenesis and (2) a piezoelectric printhead with fast pressure ramps and direct bioink aspiration/extrusion. **C.** MAGIC matrix comprises of an inert alginate microgel granular support and a viscous basement membrane interstitium. This compositionally simple material acts as a yield-stress embedded bioprinting medium at 4 °C while supporting complex tissue morphogenesis at 37 ˚C. Confocal microscopy images showing a standard MAGIC matrix composition using FITC-alginate microgels and NHS-labeled Matrigel. Scale bar = 100 μm. Zoomed view shows white pixels where fluorescent signals overlap, suggesting ECM in alginate microgels. Scale bar = 40 μm. **D.** Organoid slurries printed into liquid Matrigel at 4 °C distort and settle to the bottom of the dish due to insufficient mechanical support. Organoid bioink printed into MAGIC matrix at 4 °C conforms to the desired morphology due to the support's reversible yield-stress properties. **E.** Sequential brightfield images demonstrating MAGIC matrix bioprinting, in which the printhead enters cold MAGIC matrix, extrudes organoid slurry, and is then removed from the matrix, leaving a geometrically and spatially controlled feature behind. These organoid bioinks subsequently undergo self-organization at 37 ˚C to form mature organoids. Scale bars = 500 μm.

yield-stress properties of microgels with the mechanical and biochemical properties of basement membrane extracts could revolutionize bioprinting for generation of reproducible organoid arrays or advanced 3D microphysiological systems (Fig. 1B).

Here we designed and optimized an embedded bioprinting material that comprises alginate microgels and interstitial Matrigel, termed Matrigel-Alginate Granular-Interstitial Composite (MAGIC) matrix (Fig. 1C). MAGIC matrices employ alginate microgels that are optically transparent and approximately cell-sized, which facilitated yielding behavior, high print fidelity, imaging, and organoid expansion. We concurrently used Matrigel as the interstitial material to create a switchable composite matrix that remains liquid at 4 °C to allow for long print times (≥3 h), but cross-links at 37 °C to create a soft, viscoelastic, and viscoplastic environment that is mechanically similar to pure Matrigel across several metrics. To capitalize on the reproducibility, scalability, and automation afforded by 3D printing, we designed a piezoelectric printhead that is linked to a microscope stage and robotic arms that allow for full xyz-control, real-time imaging, and flexible scripted print geometries (Fig. 1B). This printhead enabled direct aspiration and extrusion of saturated cell slurries exceeding 10^{8} cells/mL (Fig 1D), minimizing dead volume and required biomass, with a theoretical limit of 0.1 nL delivered volume. This led to orders-of-magnitude improvements in inter-organoid homogeneity and statistical power with approximately 100% organoid formation efficiency (Fig. 1E). The combined result is a flexible 3D bioprinting platform using a simple but powerful biomaterial that can generate reproducible yet complex in vitro tissues.

Results

MAGIC matrices are designed to be optimal bioprinting materials at 4 °C and optimal tissue culture materials at 37 °C

We first sought to design a reversible yield-stress material that supports bioprinting at 4 ˚C and matches the gold-standard in morphogenesis at 37 ˚C. We turned to alginate as an optically transparent biomaterial that is largely inert in mammalian culture. For these reasons, alginate has been employed in both bioprinting and organoid culture applications as a support medium and rheological modifier[62–64]. Given our design constraints, we hypothesized that a yield-stress matrix utilizing alginate microgels with interstitial Matrigel would allow for high-fidelity bioprinting at 4 °C and optimal organoid morphogenesis at 37 °C. We termed this material Matrigel-Alginate Granular-Interstitial Composite (MAGIC) matrix.

We characterized MAGIC matrices by shear rheology under conditions relevant for bioprinting (4 ˚C) and organoid culture (37 ˚C). We explored matrix compositions having mechanical properties spanning those likely to support both bioprinting and morphogenesis. In addition to pure formulations of alginate and Matrigel we tested six different matrix compositions in total: three different ratios of Matrigel and alginate microgel (AMG) slurry spanning 2:1, 1:1, and 1:2 by volume; and two different polymer weight fractions in the AMG preparation, 0.5 and 1 wt%. As expected, pure AMG slurries exhibited temperature-independent, but shear stress-dependent viscoelasticity, including yielding at ~10 Pa shear stress for 0.5 wt% AMGs (Extended Data Fig. 1). In contrast, pure Matrigel exhibits significant temperature-dependence as it cross-links to form a hydrogel at physiological temperature (Extended Data Fig. 1).

All compositions of MAGIC matrix demonstrated reversible yield-stress behavior at 4 °C, confirming their utility as embedded bioprinting materials (Fig. 2A, Extended Data Fig. 1). At rest, they behaved as viscoelastic solids, with G' greater than G'', in contrast to pure Matrigel (Extended Data Fig. 1). However, as shear stress was increased, G'' overtook G', indicating microgel yielding and rearrangement (Fig. 2A). These materials remained as reversible yield-stress fluids for as long as they were kept cold, suggesting their ability to support long print times. The specific yield-stress of each composition was measured by unidirectional shear tests and fit well to a Herschel-Bulkley exponential model (Extended Data Fig. 1). Despite their molecular similarity, varying MAGIC matrix composition tuned yield-stress values over an order of magnitude (Fig. 2B, Extended Data Fig. 1). This implies that the material can be engineered to fit the needs of a particular print or tissue type.

To assess MAGIC matrix behavior under physiological conditions, we next measured viscoelastic properties following cross-linking at 37 °C. At 0.5 wt% alginate, the storage and loss modulus of the composite matrix approached equivalent values to pure Matrigel (Fig. 2C). This was true across a range of MAGIC matrix

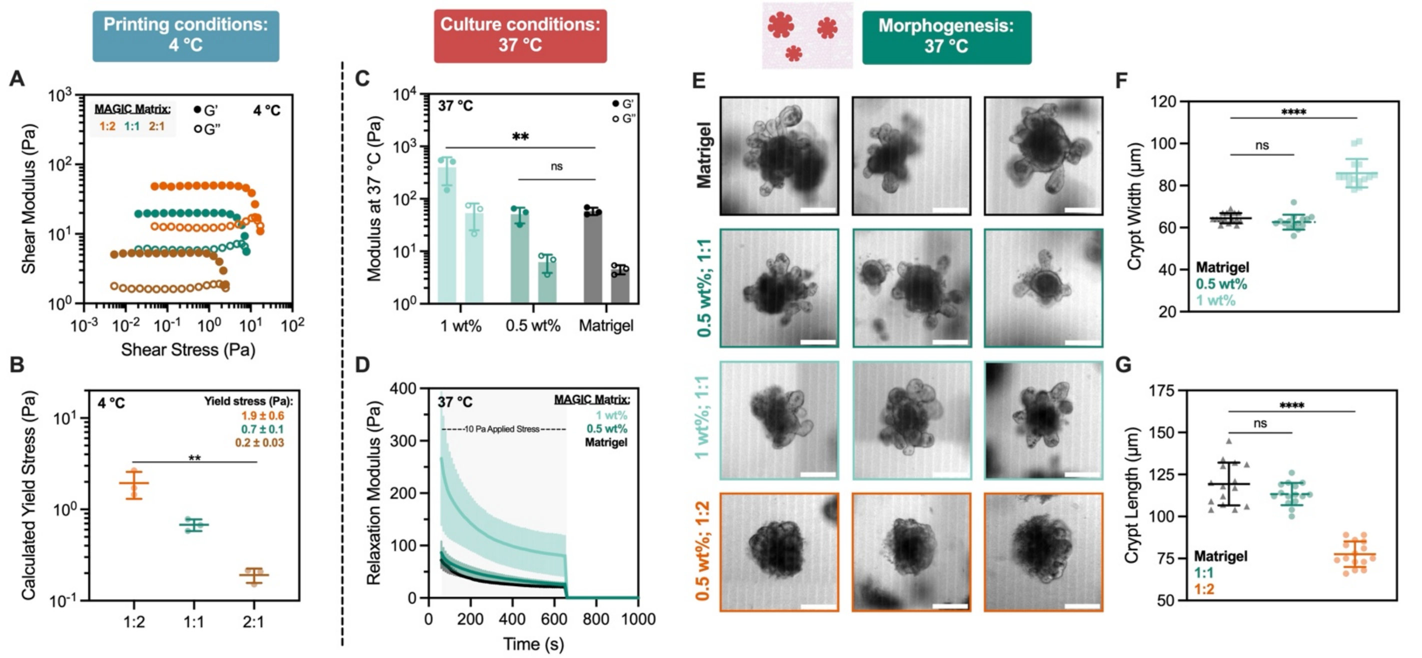

Figure 2. MAGIC matrices behave as reversible yield-stress materials at 4 °C and as viscoelastic and viscoplastic cell culture matrices at 37 °C. A. At 4 °C, oscillatory amplitude sweeps at 1 Hz reveal that various MAGIC matrix compositions behave as yield-stress materials, indicated by G' and G'' cross-over. **B.** MAGIC matrices behave as Herschel-Bulkley fluids at 4 °C with yield-stresses calculated using a power law model. **C.** Storage and loss moduli at 1 Hz and 1% strain of MAGIC matrices at 37 °C prepared from 1 wt% or 0.5 wt% AMGs. **D.** Creep experiments quantified as stress relaxation curves at constant applied stress. **E.** Mouse intestinal organoids grown in pure Matrigel (top row) and MAGIC matrices of several compositions (lower rows) five days after seeding. Scale bars = 200 µm. **F.** Quantification of organoid crypt width as a function of matrix composition. **G.** Quantification of crypt length as a function of matrix composition. For all rheological experiments, data shown are mean ± SD from n = 3 independently prepared replicates. For crypt length measurements, data shown are mean ± SD on the median n = 15 crypts from ≥10 organoids per matrix condition. ** = $p \le 0.01$; **** = $p \le 0.0001$; ns = not significant determined by one-way ANOVA with Tukey's multiple comparisons (**B**, **C**) or Dunnett's multiple comparisons (**F**).

compositions using the lower alginate weight fraction (Extended Data Fig. 1), implying that for these formulations, composite mechanics are dominated by cross-linked Matrigel. However, this was not the case with MAGIC matrices composed of 1 wt% AMGs, where viscoelastic properties were dominated by the microgel slurry (Fig. 2C, Extended Data Fig. 1). Given their similarity to pure Matrigel, the 0.5 wt% MAGIC matrix formulations were notably softer than many traditional bioprinting and biomaterial scaffolds[55], suggesting their utility for supporting tissue growth and morphogenesis.

Matrigel and other basement membrane extracts also exhibit complex mechanical behaviors such as stress relaxation and viscoplasticity over the time scales of tissue growth[55,65]. Thus, we hypothesized that these time-dependent behaviors might play a role in bioprinted organoid morphogenesis. We therefore measured the creep response of MAGIC matrices at 37 °C using 10 Pa applied shear stress over 10 minutes to simulate the forces and timescales of processes such as lumen expansion and crypt budding[59,66]. Indeed, the creep response was a strong function of material composition, with Matrigel exhibiting the greatest strain rate and highest plasticity (Extended Data Fig. 2). MAGIC matrices comprising soft (0.5 wt%) AMGs, regardless of composition ratio, exhibited similar strain rates that were less than pure Matrigel, but greater than MAGIC matrices comprising stiff (1 wt%) microgels (Extended Data Fig. 2). The corresponding relaxation modulus was nearly identical to Matrigel for MAGIC matrices using soft AMGs (Fig. 2D). In contrast, stress relaxation was substantially impeded compared to Matrigel for MAGIC matrices using stiff AMGs (Fig. 2D).

To arrive at an ideal MAGIC matrix formulation for both bioprinting and morphogenesis, we applied these ECM compositions to organoid growth assays. Organoids isolated from mouse duodenum were passaged by mechanical dissociation and plated in Matrigel or MAGIC matrix domes. Given the sensitivity of crypt budding and lumen expansion to matrix mechanics[10,18,59,67], we measured crypt width and length as representative signatures of a permissive ECM and healthy morphogenesis. After five days in culture, we found that MAGIC matrix compositions employing 0.5 wt% alginate gels at low enough packing density yielded organoids that were indistinguishable from those grown in pure Matrigel (Fig. 2E). However, all compositions of MAGIC matrix using 1 wt% AMGs yielded organoids with shorter and wider crypts (Fig. 2F). We also observed a negative impact on crypt length for MAGIC matrices composed of 0.5 wt% soft microgels for a high microgel-fraction composition, namely 1:2 Matrigel:AMG by added volume (Fig. 2G). Given that these materials have similar viscoelasticity at 37 °C (Fig. 2C), and that organoids exhibit standard morphology in diluted Matrigel (Extended Data Fig. 3), it is possible that microgel packing may also play a role in organoid phenotype. In sum, the formulations that were most mechanically similar to pure Matrigel showed no significant impact on crypt morphogenesis (Extended Data Fig. 3). These results support the need for soft, viscoelastic materials for embedded bioprinting to promote certain aspects of morphogenesis. In addition, they suggest that for MAGIC matrices of a given storage and loss moduli, other material properties such as time-dependent viscoelasticity, plasticity, and microgel packing may independently inform intestinal organoid morphogenesis. For most bioprinting experiments, unless otherwise noted, we used our standard MAGIC matrix composite with a 1:1 ratio by added volume of Matrigel and 0.5 wt% AMGs.

A piezoelectric printhead enables precise, automated aspiration and extrusion of dense cell slurries

Our group and others have demonstrated that organoid morphogenesis can be highly stereotyped when cells are embedded in physiologically relevant matrices at tissue-like cell densities[22,41,48,53]. We therefore focused our efforts on bioinks comprising single-cell suspensions of dissociated organoids centrifuged to produce saturated slurries at approximately 10^8 cells/mL[40,68,69]. We omitted rheological modifiers and generally excluded divalent cations to temporarily prevent cell adhesion through calcium-dependent adhesion molecules. In addition, we employed microgels that were approximately cell-sized to facilitate self-organization, migration, and diffusion[53,70] (Extended Data Fig. 4). However, we found that reproducible and controlled printing of cell slurries at these densities required a printhead that could handle small volumes with high precision, fast pressure ramps, and without excess loss due to tubing and fluidics (i.e. “dead volume”). Thus, we designed a printhead for direct aspiration and extrusion that employs a piezoelectric actuator that is mechanically coupled to a fluid-filled cavity via a polyether ether ketone (PEEK) diaphragm (Fig. 1B). This allowed voltage applied to the piezoelectric material to control its expansion or contraction, and thus both aspirate and dispense precise volumes. The chosen piezoelectric actuator, PEEK diaphragm diameter and diaphragm thickness result in a volume displacement resolution of approximately 10 pL, a maximum aspiration/extrusion volume of approximately 660 nL, and a maximum theoretical aspiration/extrusion rate of approximately 300 µL/s (the actual rate will be highly dependent on the bioink rheological properties).

The piezoelectric printhead was mounted on a cantilevered beam, with motorized Z-control but a fixed XY-position. The printhead can be aligned to the optical axis of the widefield microscope with manual centering screws. Micron-scale resolution of xy-position and shape was achieved using the microscope stage, which held the print plate. Microscope integration provided real-time imaging during the printing process, which allowed rapid identification and diagnosis of printing issues should they occur. Bioinks were loaded by directly aspirating a user-specified volume from a 384-well sample plate, so that only the printed volume was loaded – this is especially beneficial for precious samples such as biopsies or cell populations with insufficient bioink volume for loading typical commercial bioprinting syringes. A solenoid valve toggled fluidic connection of the printhead cavity to a fluid reservoir, allowing the printhead to be filled, cleaned, or purged, and then sealed for single-ended printing operation. The entire process, including microscope, printer motion, and fluidics, were controlled using MATLAB. Custom printing protocols were scripted for maximum repeatability, efficiency, and iterative troubleshooting (Supplementary Movie 2).

High-viscosity ink droplets are challenging to print in yield-stress fluids due to inertial, cohesive, and shear forces between the ink and matrix[71,72]. For example, cohesive interactions between cells in the slurry causes the ink to be pulled as a continuous tail from the tip as it is removed from the bath, generating a structure reminiscent of capillary bridging[73,74]. To combat this, we leveraged a rapid voltage switch on the piezo printhead to “break” this tail by applying a small negative pressure and xz-displacement, generally attenuating this effect (Fig. 3A–B). We then applied this aspiration, extrusion, and tail-breaking program to script an automated spheroid bioprinting array. Using commercially available plastic micropipettes with 1 mm OD and 125 µm ID mounted onto the printhead, we first demonstrated that a Caco-2 cell slurry bioink could be delivered to create spheroids (Fig. 3C) of customizable dimensions. Spheroid area was an approximately linear function of extrusion step, which was controlled through changes in voltage applied to the piezoelectric actuator (Fig. 3D).

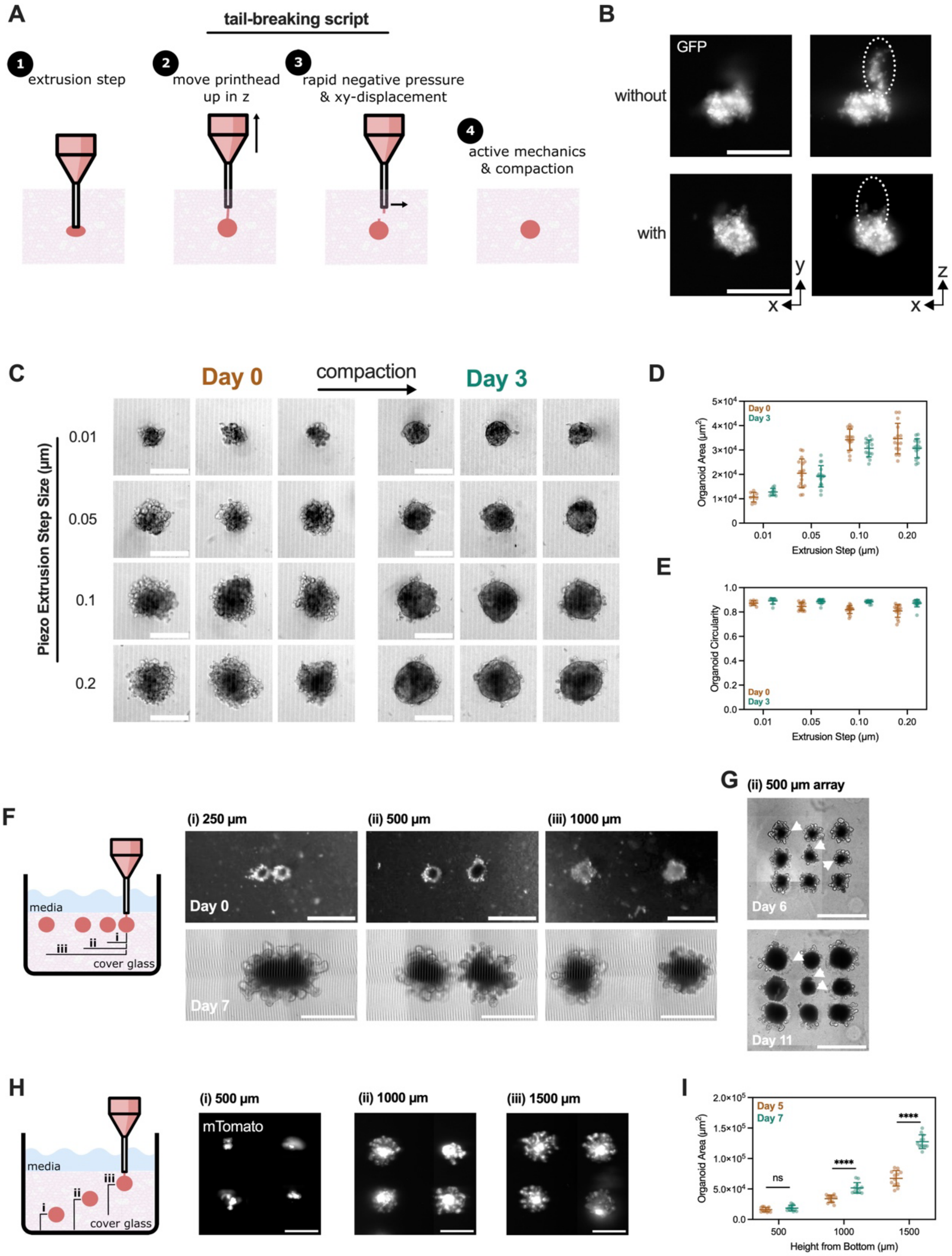

Figure 3. A piezoelectric printhead enables precise aspiration and extrusion of cell slurries and can be programmed to generate automated organoid arrays. **A.** The piezoelectric printhead and precise xyz-control tolerate rapid pressure ramps and print plate movement, enabling scripts such as tail-breaking to improve print fidelity of viscous cell slurry bioinks. **B.** Representative fluorescent images of bioprinted spheroids with and without a tail-breaking script enabled by piezoelectric bioprinting through rapid changes in applied voltage and printhead position. Scale bars = 200 µm. **C.** Representative brightfield images of bioprinted Caco-2 tissues at day 0 and day 3 post-print as a function of extrusion step size controlled via applied voltage. Data are representative of at least n = 9 individual tissues per extrusion step condition, scale bars = 200 µm. **D.** Organoid area and **E.** circularity measured using max intensity projections of confocal z-stack images of GFP-expressing Caco-2 cell slurries. At both day 0 and day 3, organoid area significantly depends on extrusion step size until beyond 1.0 µm as determined by one-way ANOVA with Tukey's multiple comparisons. Data shown are mean ± SEM of n ≥ 9 individual tissues per extrusion condition. At day 3, organoid circularity does not depend significantly on extrusion step size as determined by one-way ANOVA. **F.** Bioprinted mouse intestinal organoid pairs printed with 250, 500, or 1000 µm center-to-center organoid spacing. Tissues printed close together (~75 µm edge-to-edge) fuse (i), whereas tissues printed far enough apart (>~300 µm edge-to-edge) don't fuse (ii, iii). Scale bars = 500 µm. **G.** Organoids printed in arrays with 500 µm pitch lack crypts between day 6 and 11. Carrots indicate crypts formed close to the neighboring organoids that are gone by day 11. Scale bars = 500 µm. **H.** Maximum intensity projections of intestinal organoid arrays bioprinted at different depths within the MAGIC matrix (500 µm, 1000 µm, or 1500 µm from the cover glass). Scale bars = 500 µm. **I.** Organoids printed deeper in the matrix (i) do not significantly grow between days 5 and 7 post-print compared to organoids printed closer to the media interface (ii, iii). Data shown are mean ± SD of n = 12 organoids per condition; ns = not significant, **** = p < 0.0001 determined by non-parametric t-test between day 5 and day 7.

In general, around 90% of cells were viable after dissociation and slurry preparation as measured by trypan blue exclusion. In addition, Caco-2 spheroids underwent lumenization, as is expected for these tissues in 3D culture[75], implying the dissociation and printing process did not substantially impact morphogenesis. Notably, the high viscosity of cell slurry bioinks negatively impacted print circularity for larger extrusion steps; however, the active rheological behavior of these living inks can overcome imperfections in initial geometry, highlighting the benefits of self-organizing systems as living inks (Fig. 3E). Cell slurry could also be printed using 75 or 200 µm ID micropipettes, highlighting the flexibly of the platform for various print resolutions. Thus, the piezoelectric printhead affords high volume precision, working with small volumes of precious cellular inks, and flexible control over bioink behavior by rapidly changing applied voltage. To our knowledge, this is the first demonstration of applying a piezoelectric material to control direct aspiration and extrusion of dense cell slurries.

Having established conditions for the automated preparation of 3D tissues using Caco-2 cells, we next bioprinted mouse small intestine organoid arrays. Primary cells were harvested, cultured, passaged, and dissociated into a cell slurry as previously described[48]. We hypothesized that a significant contributor to organoid heterogeneity in traditional ECM dome cultures is the disparity in extrinsic conditions such as media access or inter-organoid spacing. To assess the impact of initial spatial conditions on organoid growth, we systematically varied either inter-organoid spacing or z-depth within the MAGIC matrix support bath. Organoid were printed with an average diameter of 200 µm. Organoid seed pairs printed with 250 µm inter-bolus spacing fused over time, leading to one large organoid (Fig. 3F). This fusion is known to occur in manually seeded ECM dome culture[18,41]. Organoids spaced 500 or 1000 µm apart remained distinct and appeared to undergo normal morphogenesis through at least 7 days of culture (Fig. 3F). To test denser organoid seeding densities, 3 x 3 arrays with 500 µm spacing were printed. Notably, after 11 days in culture, crypts only appeared at the periphery of the organoid array, while the central organoid remained compacted and showed signs of cell death (Fig. 3G). We hypothesize that this could be caused either by nutrient depletion by outermost organoids or autocrine gradients. Printing depth also had a profound effect on organoid health, with organoids printed closer to the ECM-media interface growing the largest and forming the most crypts (Fig. 3H)[76]. Organoids printed too far from the ECM-media interface did not significantly grow over the same time (Fig. 3I). Together, these results highlight the importance of initial conditions on organoid morphogenesis and imply that these effects could impact experimental results when working with organoids in manual 3D culture. Ultimately, the automation and standardization afforded using the piezoelectric printhead and MAGIC matrices allows rapid exploration of a wide parameter space and initial culture conditions tailored for a desired assay or application.

Flexible production of 3D perfusable organoid tubes

In addition to enabling more rapid and homogeneous formation of organoids in a standard array format, MAGIC matrices and the piezoelectric printhead present opportunities to create more structurally complex and functional 3D tissues from organoid slurries. One architecture common to many tissue types is a tubular geometry. Many tissues spontaneously lumenize to form tubes from an initially cylindrical morphology when placed in laminin-rich ECM[41,47,48]. We therefore optimized process parameters for bioprinting organoid cylinders, with the hypothesis that MAGIC matrices would support their spontaneous lumenization, and therefore, their perfusion. Using Caco-2 cell slurries, cylinder diameter could be tuned using either or both extrusion speed and stage speed, providing multiple engineering controls (Fig. 4A). Tube diameter was an approximately linear function of extrusion speed for the two stage speeds tested. Bioprinted Caco-2 cylinders underwent similar self-organization and compaction followed by lumenization as observed in spheroid arrays (Fig. 4A, insets).

Organoids and cell-dense tissues in vitro are generally limited to about 1 mm^3 in volume without vasculature[39,77,78]. Thus, generating de novo vasculature is a focus within the bioprinting community[79,80]. We validated MAGIC matrix bioprinting for generating vascular cords by preparing cell slurry bioinks from human umbilical vein endothelial cells (HUVECs) and printing them in tubular geometries. Similar to our previous work preparing vasculature from cell-dense HUVEC patterns[47], after 7 days in culture, these vascular cords exhibited signs of tube formation and microvessel sprouting when printed into MAGIC matrix compositions that additionally included 1 mg/mL Collagen I (Fig. 4B, Supplementary Movie 3). However, in contrast to this previous work, MAGIC matrix bioprinted vessels could be tuned in length and width over a greater range. These results highlight the utility of printing into MAGIC matrices having flexible composition including additives like collagen.

We next applied MAGIC matrix bioprinting to form perfusable tubular geometries with more complex local architectures, such as intestinal tubes prepared from mouse duodenal organoid bioinks. These tubes lumenized and began forming crypts radially around the long axis of the intestinal tube 2–3 days after printing (Fig. 4C, Supplementary Movie 4). The emergence of patent lumens in printed tissues provides an opportunity to interface these complex culture models with perfusion systems. Using glass capillaries piercing the tissue lumen, we pushed fluid through the tubes, clearing internal cellular debris (Fig. 4D). We observed radial expansion of the perfused tubes when pressurized, indicating that the boundaries of the tissue remained flexible, unlike cultures in materials with non-physiological stiffness such as PDMS (Fig. 4E). By applying oscillatory fluid flow through the tube, we could simulate cyclic expansion and contraction of the tubes as might occur during peristalsis (Supplementary Movie 5). Thus, MAGIC matrix tube bioprinting enables access to the apical lumen, a key feature of microphysiological systems, while maintaining a free basal surface that ultimately can be interfaced with other tissue types.

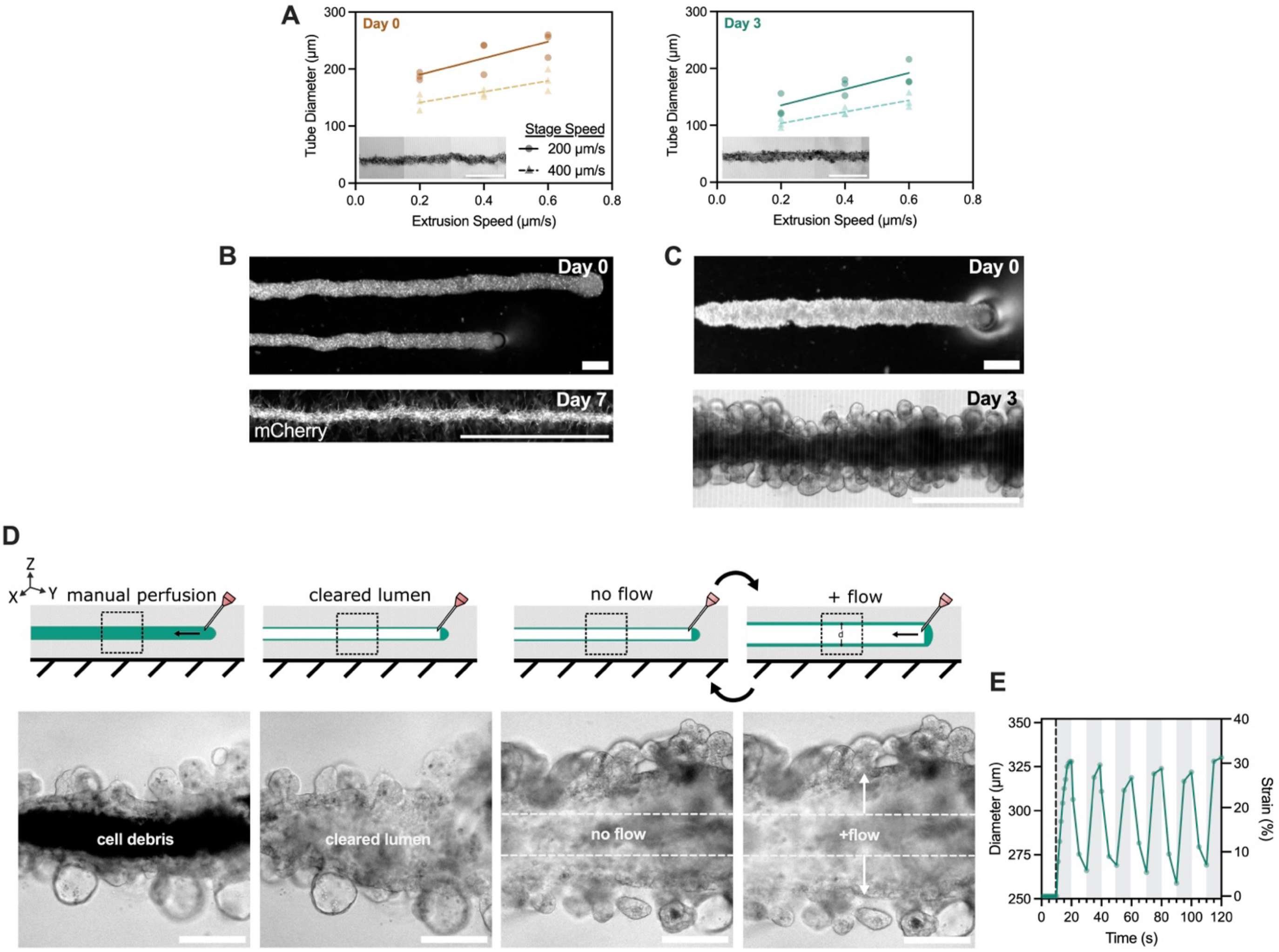

Figure 4. MAGIC matrix bioprinting of organoid tubes into perfusable 3D microphysiological systems. A. Quantification of bioprinted tube diameter at day 0 and day 3 post-printing as a function of both stage translation speed and extrusion step speed. Fit demonstrates that initial and final tube diameter are approximately linear functions of extrusion step speed for a given stage translation speed. Insets show representative brightfield images of tubes from that day; scale bar = 500 µm. Data shown are n = 3 bioprinted tubes per condition. **B.** Representative live images of bioprinted mCherry-expressing HUVEC tubes during printing (day 0) and following self-organization (day 7). Tubes over 2 mm long could be printed, with signs of vascular sprouting. Scale bars = 200 µm (day 0) and 1 mm (day 7). **C.** Representative live images of bioprinted intestinal organoid tubes during printing (day 0) and after self-organization (day 3), showing lumenization, crypt formation, and epithelial shedding. Scale bars = 200 µm (day 0) and 500 µm (day 3). **D.** Brightfield images of bioprinted intestinal organoid tubes that are manually perfused with a glass capillary attached to a micromanipulator and flushed to get rid of cell debris and access the lumen. Scale bars = 200 µm. **E.** Quantification of tube diameter and resulting strain upon application and removal of fluid flow. Gray bars correspond to times when fluid flow was applied.

MAGIC matrix supports rapid self-organization of many organoid types following bioprinting

Having established initial conditions supporting controlled organoid growth, we next assessed whether organoid arrays from various developmental lineages cultured in MAGIC matrix exhibited characteristic features of their self-organization. We assessed the morphology of organoids using confocal microscopy, taking advantage of the optical transparency of the matrix and the consistent z-position of all organoids in a printed array. For mouse duodenal organoids, live imaging of a membrane-localized tdTomato reporter revealed crypt budding and protrusion within 2–3 days after printing in 96-well microplates (Extended Data Fig. 5). In these folded outgrowths of the epithelium, *Lgr5*+ stem cells were effectively positioned toward the base of the folded structures (Fig. 5A). Fixed intestinal organoids stained positive for mature epithelial cell types, including Paneth cells (lysozyme) and enteroendocrine cells (chromogranin-A) (Fig. 5A, Extended Data Fig. 5). Cohesive and contiguous cell borders were marked with E-cadherin. Bioprinted intestinal organoid tubes showed similar self-organization and were positive for Paneth cells (Fig. 5B). 3D reconstruction of organoids in MAGIC matrix revealed that crypts radiated in all directions from the organoid, suggestive of 3D morphogenesis unencumbered by neighboring interfaces (Fig. 5A, Extended Data Fig. 5).

To establish the generality of MAGIC matrix for bioprinting and morphogenesis of tissues from different developmental lineages, we derived organoids from mouse submandibular salivary gland, an ectoderm-derived tissue. These organoids were cultured in Matrigel domes and then harvested as a single-cell slurry in an identical fashion to the small intestine organoids (Extended Data Fig. 5). Bioprinted salivary gland organoid arrays self-organized and exhibited characteristic multi-lobular structures within 3 days of printing. These organoids expressed ductal and basal epithelial markers, keratins 8 and 14, respectively.

Self-organization occurs in a variety of contexts with different mechanisms, including sorting based on differences in cell-cell and cell-ECM interfacial interactions[81,82]. Given that organoid bioinks are dissociated and mixed before bioprinting, we aimed to test whether cells retain the ability to sort after printing into the MAGIC matrix. To test this, we printed spheroid arrays of patient-derived human mammary epithelial cells (HMECs) given their robust cell sorting into bilamellar structures comprised of a core of luminal cells (LEP) and an outer layer of myoepithelial cells (MEP)[22,83] (Fig. 5C). We confirmed that the printed tissues robustly sort to form bilamellar structures within one day, and the extent of MEP coverage was dependent on the proportion of the two cell types (Fig. 5D). Additionally, we also confirmed that HMEC printed as tubes also sort robustly while maintaining the initial tissue geometry. In contrast, MEP-only spheroids showed no evidence of sorting (Fig. 5D). Thus, MAGIC matrix bioprinting is compatible with a variety of self-organization mechanisms, including sorting, lumenization, and tissue folding.

The most common approach for preparing many organoid types is to aggregate dissociated tissue or stem cells using low attachment wells. However, these methods frequently lead to uncontrolled spheroid formation and a field of unincorporated or dead cells at the periphery of the organoids. Furthermore, while these organoid seeds appear to coarsen over time, it is unclear how these dynamics impact tissue organization (Fig. 5E). We reasoned that MAGIC matrix bioprinting could attenuate this effect by providing a mechanical support during tissue formation. To test this idea we explored the feasibility of bioprinting human induced pluripotent stem cell (hiPSC)-derived forebrain organoids[84,85]. Specifically, brain organoids at 7 weeks of in vitro differentiation were dissociated into a cell slurry bioink and printed into both MAGIC matrix or a pure AMG slurry and assessed for rosette formation and neural identity. Cortical brain organoids printed into MAGIC matrix exhibited sprouting behavior that is known to occur in basement membrane gels, as well as neuroepithelial bud formation, but lacked neuroectoderm (Extended Data Fig. 6)[86,87]. In contrast, cortical brain organoids printed in pure AMG slurry formed dense spheroids without surrounding cell debris that exhibited radially organized neuroectoderm (Fig. 5E). These organoids were positive for the dorsal forebrain marker *FOXG1* and negative for the ventral forebrain marker *DLX2*, with about 40% dorsal identity, comparable to hiPSC-derived cortical organoids aggregated with low attachment wells and not bioprinted (Fig. 5F). Furthermore, the bioprinted cortical organoids demonstrated characteristic self-organization with neural progenitors surrounding ventricular zone-like neuroepithelium regions (PAX6+, ~30%), and intermediate progenitor cells (EOMES+, ~4%) and deep layer excitatory neurons (CTIP2+, ~15%) extending radially out from this apical surface (Fig. 5F). Bioprinted organoids showed similar cell proportions to manually seeded organoids, except for a decreased PAX6+ population, likely

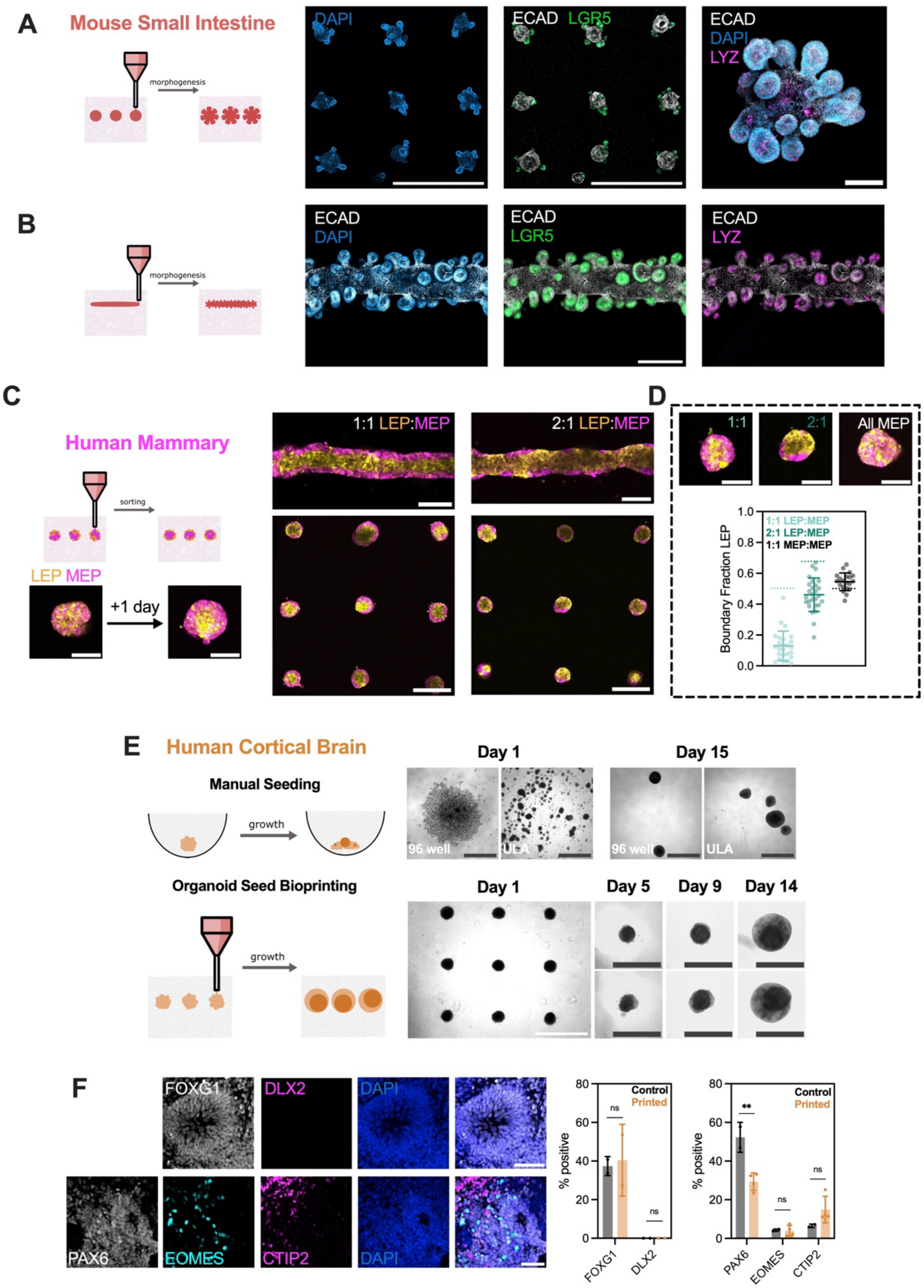
A
Mouse Small Intestine
morphogenesis
DAPI
ECAD LGR5
ECAD
DAPI
LYZ
B
morphogenesis
ECAD
DAPI
ECAD
LGR5
ECAD
LYZ
C
Human Mammary
sorting
LEP MEP
+1 day
1:1 LEP:MEP
2:1 LEP:MEP
D
1:1
2:1
All MEP
1:1 LEP:MEP
2:1 LEP:MEP
1:1 MEP:MEP
Boundary Fraction LEP
1.0
0.8
0.6
0.4
0.2
0.0
E
Human Cortical Brain
Manual Seeding
growth
Day 1
Day 15
96 well
ULA
96 well
ULA
Organoid Seed Bioprinting
growth
Day 1
Day 5
Day 9
Day 14
F
FOXG1
DLX2
DAPI
PAX6
EOMES
CTIP2
DAPI
% positive
80
60
40
20
0
Control
Printed
ns
ns
FOXG1
DLX2
% positive
80
60
40
20
0
Control
Printed
**
ns
ns
PAX6
EOMES
CTIP2

Figure 5. MAGIC matrices promote self-organization of organoids derived from the three primary germ layers. A. Maximum intensity projections of DAPI- (left) or ECAD- and GFP-stained (middle) intestinal organoid arrays 3 days after bioprinting. Scale bar = 1 mm. 3D rendering of one bioprinted organoid stained for DAPI, ECAD, and Paneth cells (LYZ) demonstrating radial extension of crypts in 3D. Scale bar = 100 µm. **B.** Staining as in (A) of bioprinted intestinal organoid tubes 3 days after bioprinting. **C.** Maximum intensity projections of bioprinted spheroid arrays and tubes of human mammary epithelial cell (HMEC) organoids of different luminal and myoepithelial compositions. Organoids were allowed to sort for one day following printing. Scale bars = 500 µm for arrays and tubes; scale bars = 200 µm for individual spheroids. **D.** Representative live images and quantification of luminal cell boundary occupation in bioprinted organoids as a function of composition. Dashed lines represent expected boundary occupancy for mechanically equivalent cells[22]. Data shown are mean ± SD for n ≥ 20 organoids analyzed per composition. Scale bars = 200 µm. **E.** Comparison of manually seeded and bioprinted induced pluripotent stem cell-derived human cortical brain organoids. Brightfield images of manually seeded cortical brain organoids in 96 or ultra-low attachment (ULA) well plates (top) or bioprinted arrays (bottom) over time. Scale bars = 1 mm (array) or 200 µm (manually seeded or individual bioprinted organoids). **F.** Left, 20 µm maximum intensity projections of bioprinted cortical organoids stained for cortical identity (top) and neuronal differentiation (bottom). Scale bars = 50 µm. Right, quantification of cortical identity and neuronal differentiation compared to manually seeded cortical brain organoids. Data shown are mean ± SD of n = 2 or 3 organoids per marker; ns = not significant, ** = p < 0.01 as determined by non-parametric t-test.

due to increased organoid age in bioprinted organoids (63 d) compared to manually seeded (39 d). Together, these results validate organoid bioprinting for hiPSC-derived tissues and lay the groundwork for generating more complex organoid interfaces such as neural assembloids[88].

Generation of high-throughput bioprinted organoid arrays for assay development

Similar to aggrewell or microwell methods, bioprinted organoid arrays hold great promise for high-throughput assay development, CRISPR libraries, and drug screens. However, there is the added benefit of flexibility in tissue geometry and initial conditions. To explore the utility of MAGIC matrix for assays requiring genetic perturbations, like CRISPR screens, we transduced triple-negative breast cancer (TNBC) patient-derived organoids using lentivirus expressing H2B-GFP (Fig. 6A). TNBC organoids showed no difference in infection efficiency when transduced in suspension and then plated in Matrigel or MAGIC matrix domes (Fig. 6B). However, when transducing TNBC organoids through the ECM domes by including lentivirus in the media after plating and gel cross-linking, infection efficiency was significantly greater in MAGIC matrix, with nearly 90% GFP+ organoids. In contrast, there was minimal-to-no infection in Matrigel. We hypothesize this is due to improved diffusivity afforded by low wt% (and therefore large pore size) alginate microgels in the composite support. These results implied that TNBC organoids could be transduced after printing in arrays, presenting opportunities to multiplex combinatorial libraries in a single well plate. To this end, surface cells on TNBC organoids could be successfully transduced by including lentivirus in the media after bioprinting (Fig. 6C). Bioprinted TNBC organoid arrays were also highly amenable to transfection using Lipofectamine, showing strong RNA uptake as a function of both transfection time and amount of RNA delivered (Fig. 6C, Extended Data Fig. 7). While transduction efficiency in bioprinted arrays could be improved, this provides an important proof-of-concept for future assays using patient-derived organoids in this format.

Achieving regularity for organoids with complex morphogenetic features is a key challenge in developing organoid-based assays, as it effects the response of the organoids to genetic, mechanical and chemical perturbations. For examples, crypt morphogenesis in mouse small intestinal organoids is highly chemo- and mechanosensitive[10,89]. We therefore quantified the timing and regularity of crypt morphogenesis after bioprinting in MAGIC matrix compared to manual culture methods. Over the course of 5 days, bioprinted organoids synchronously self-organized, initially into lumenized cysts that further underwent budding morphogenesis to form crypts (Fig. 6D). By contrast, manually seeded organoids showed far more heterogeneous sizes and morphologies over the same timeframe (Fig. 6E). Furthermore, for a given time post-seeding, bioprinted organoid arrays underwent more extensive and uniform morphogenesis, exhibiting a greater number of crypts with decreased variance compared to manually seeded organoids (Fig. 6F)[90]. Organoids grown in manually seeded cultures using MAGIC matrix as opposed to pure Matrigel showed no difference in crypt number, indicating that the controlled initial conditions afforded by bioprinting leads to this improved maturity.

Bioprinted organoid arrays dramatically improve assay statistical power

The heterogeneity of manually seeded organoid culture limits their potential in a variety of phenotypic assays. Differences in organoid size, morphological features such as number of crypts, and position across multiple z-planes obscures subtle phenotypes that are only revealed after analyzing dozens to hundreds of individual organoids. The regularity of bioprinted organoid arrays in MAGIC matrix could dramatically improve the sensitivity of such assays while reducing input tissue. To test this idea, we treated intestinal organoids with a gamma-secretase inhibitor, N-[N-(3,5-Difluorophenacetyl)-L-alanyl]-S-phenylglycine t-butyl ester (DAPT), which is known to increase the number of *Atoh1*+ secretory progenitors[91,92]. Using an $\mathit{Atoh1}^{\mathit{CreERT2}}$:$\mathit{Rosa26}^{\mathit{tdTomato}}$ reporter line, we treated bioprinted and manually seeded organoid cultures with DAPT for 2 days after seeding and imaged after 3 days (Fig. 6G). In manually seeded organoids, differences in overall tdTomato signal acquired by confocal microscopy were obscured by heterogeneity in organoid position and size (Fig. 6H). In contrast, there was a clear increase in tdTomato signal for DAPT-treated organoids in bioprinted arrays (Fig. 6I). Quantifying the volume of tdTomato-positive signal in each condition revealed that while there was a statistically significant increase in signal for both bioprinted and manually seeded organoids in treated vs. untreated conditions, the effect size was substantially improved using bioprinted arrays (~3.7-fold increased difference between treated and untreated means) (Fig. 6J). Signal-positive volumes were also not normally

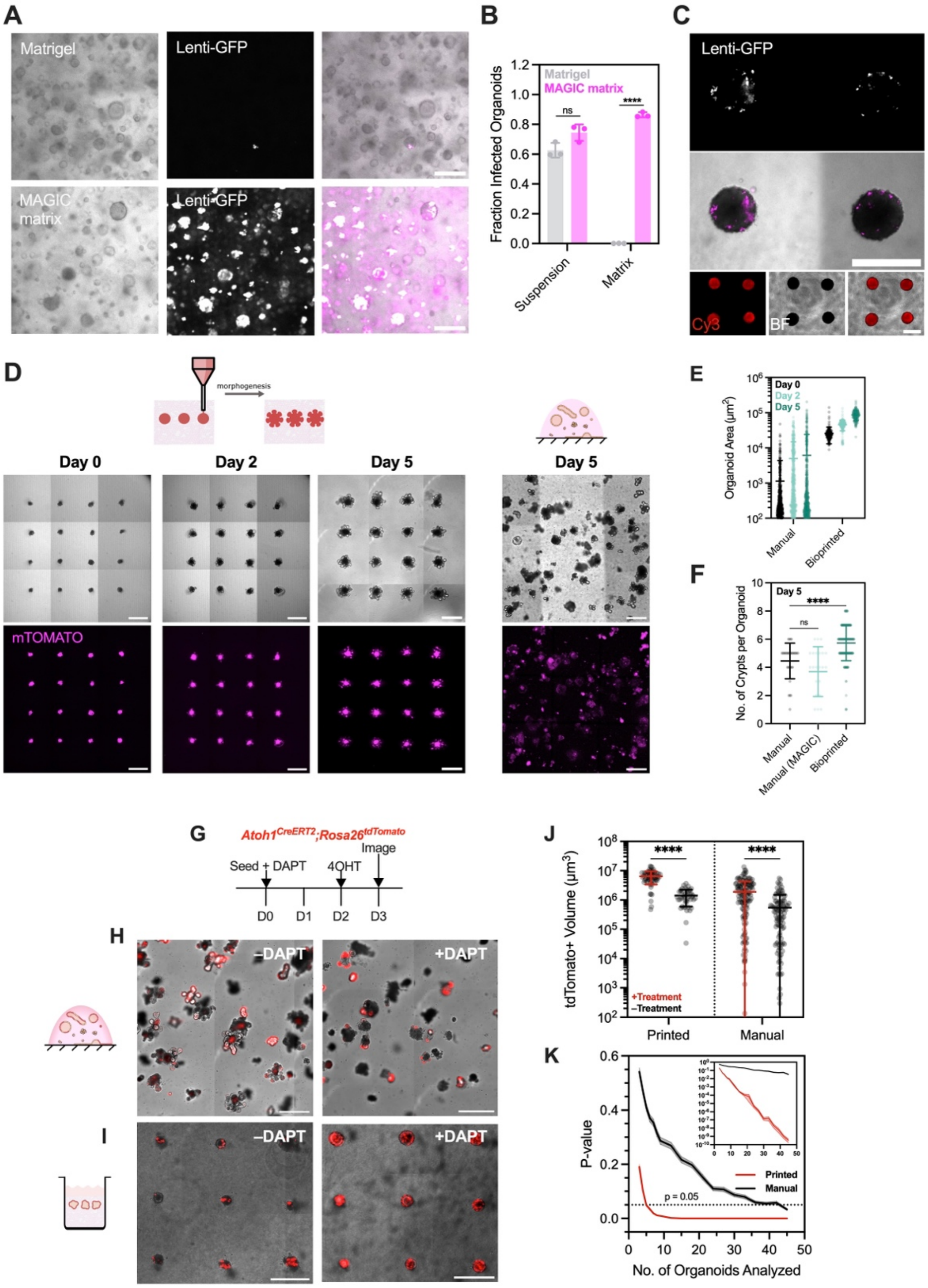

Figure 6. High-throughput bioprinting of organoid arrays decreases heterogeneity and improves assay statistical power. **A.** Live images of triple-negative breast cancer (TNBC) patient-derived organoids transduced overnight with GFP-expressing lentivirus while seeded in Matrigel (top) or MAGIC matrix (bottom). Scale bars = 200 µm. **B.** Fraction of GFP+ organoids transduced in suspension before seeding or transduced after seeding for either ECM composition. Data shown are mean ± SD of n = 3 replicate ECM conditions; ns = not significant, **** = $p < 0.001$ determined by non-parametric t-test between ECM conditions. **C.** Live images of bioprinted TNBC organoids transduced with GFP-expressing lentivirus overnight after printing (top) or transfected using Lipofectamine and Cy3-conjugated single-stranded non-coding small RNA for 24 h, 3 days after printing (bottom). Scale bars = 500 µm. **D.** (Left) Live imaging of bioprinted intestinal organoid arrays following printing and after 2 and 5 days in culture. (Right) Live imaging of manually seeded organoids after 5 days of culture. Scale bars = 500 µm. **E.** Organoid area over time for manual or bioprinted intestinal organoids; data shown are mean ± SD of n ≥ 190 organoids per time point. **F.** Quantification of crypts per organoid for those manually seeded in Matrigel or MAGIC matrix, or bioprinted. Data shown are mean ± SD of n ≥ 30 organoids; ns = not significant; **** = $p < 0.0001$ determined by one-way ANOVA with Dunnett's multiple comparisons. **G.** Experimental outline of phenotypic assay for inhibition of gamma-secretase. **H, I.** Live imaging of manually seeded (top) and bioprinted (bottom) organoids treated with and without gamma-secretase inhibitor. Red fluorescence indicates *Atoh1*+ secretory progenitors. Scale bars = 500 µm. **J.** Total red fluorescence volume per organoid in treated and untreated conditions. For bioprinted arrays, data shown are mean ± SD of n = 45 organoids per condition. For manually seeded organoids, data shown are mean ± SD of n ≥ 135 organoids per condition. **** = $p < 0.0001$ determined by non-parametric t-test. **K.** Bootstrapping analysis of statistical significance between treated and untreated conditions for either bioprinted or manually seeded organoids as a function of number of paired comparisons. Inset shows statistical significance approaches zero (< 10^{-9}) for bioprinted organoids using an equivalent number of comparisons as it takes manually seeded organoids to approach p = 0.05.

distributed when manually seeded ($p < 0.0001$ as determined by D'Agostino & Pearson test), whereas they were normally distributed when bioprinted, resulting in more normally distributed variance in bioprinted organoids and an order-of-magnitude decreased coefficient of variance (printed CoV = 48% for treated and 58% for untreated; manual CoV = 127% for treated and 174% for untreated). Computing a post-hoc power analysis ($\alpha = 0.05$; $\beta = 0.2$) with the given effect sizes and variances in each condition recommended n = 12 printed organoids compared to n = 100 manually seeded organoids. This order-of-magnitude decrease in required comparisons emphasizes the attractiveness of MAGIC matrix bioprinting for rare tissues or subtle phenotypes.

To more precisely quantify how bioprinted arrays improved assay sensitivity, we performed bootstrapping on the bioprinted and manually seeded populations to calculate p-value as a function of the number of paired organoid comparisons (treated vs. untreated). In the bioprinted arrays, we achieved p-values below 0.05 after comparing only 5 organoids; in manually seeded organoid cultures, 45 comparisons were required to reach the same statistical significance (Fig. 6K). P-values for bioprinted organoids continued to decrease with additional comparisons approaching $p \sim 10^{-10}$ after 45 comparisons – the same number of organoids necessary to reach a p-value of 0.05 in manually seeded organoids. This 10^{8}-fold improvement in assay sensitivity highlights the potential of organoid arrays in chemical, microenvironmental, and genetic screens.

Discussion

Through key innovations in biomaterials for embedded bioprinting and printhead design, we have created a generalizable and scalable platform for 3D organoid and tissue fabrication. In contrast to most embedded bioprinting materials optimized only to support printed shapes, we have additionally designed and optimized materials to support tissue self-organization. Our work identified the important rheological parameters necessary for a permissive growth environment. One such critical finding was that optimal MAGIC matrices were an order of magnitude softer than most synthetic matrices reported in the literature. A second was the importance of ECM relaxation upon application of stress at tissue-relevant magnitudes to support gold-standard morphogenesis. Despite their complex rheological properties, MAGIC matrices are relatively simple in design, employing off-the-shelf and well-characterized constituents. Moreover, they are readily tunable by changing the size and composition of the granular medium as well as the interstitial material. To fully utilize these materials, we developed a piezoelectric printhead that precisely aspirates and extrudes cell slurries at tissue-like densities, thereby allowing tissues to autonomously self-organize while minimizing the stochasticity typically associated with traditional manual seeding. Combined, the matrix and printhead enable rapid prototyping and controlled extrusion of delicate materials while attenuating dead volume. Importantly, the overall design allows access to combinations of extrusion rate and delivered cell volumes that are difficult or impossible to achieve using pneumatics or syringe pumps.

The size and modulus of the microgel fraction of granular media are known to impact cell growth and behavior[93,94]. Here, we demonstrate that a combination of rheological properties including plasticity, stress relaxation, and yield-stress are critical dimensions to consider when designing ECMs for bioprinting and tissue culture[95]. Given these results, we proceeded with bioprinting experiments using a MAGIC matrix composition of 1:1 Matrigel-to-AMGs by added volume prepared at 0.5 wt% alginate. These materials balanced expected intestinal organoid morphogenesis at 37 °C with a low yield-stress at 4 °C (~1 Pa) that supported both print fidelity and long-term tissue health. The yield-stress of many reported embedded printing materials is much higher than that of MAGIC, which may contribute to their ineffectiveness as cell culture materials[60]. Notably, the desired yield-stress of MAGIC matrices can be tuned for a given application independent of the bulk viscoelasticity during cell growth. In addition, the viscous, elastic, and plastic properties of alginate could be tuned independent of Matrigel chemical composition by changing the degree of cross-linking or weight fraction. Depending on the specific formulation, this may lead to changes in time-dependent stress relaxation, which provides another engineering handle for controlling tissue morphogenesis. Ultimately, the simultaneous simplicity and flexibility of this biomaterial should enable broad use for 3D culture applications.

We successfully printed both mouse and human tissues from all major germ layers, including endoderm (intestinal), ectoderm (brain; mammary; salivary gland), and mesoderm (vasculature), unified by their ability to self-organize in MAGIC matrices after dissociation. These organoids, in particular intestinal organoids, showed increased homogeneity by a number of metrics, including growth, morphogenesis, and maturation rate. In previous studies, small intestine organoids exhibiting any number of crypt structures have been deemed "assay-ready," meaning the functional epithelial cell types and morphologies are established[25]. Methods for generating organoid arrays that rely on single-cell dissociation and sorting for *Lgr5*+ stem cells generate assay-ready organoids in 5 days or more[19,25]. Comparatively, MAGIC matrix bioprinted organoids were assay-ready in 2-3 days. All organoid sources tested could be bioprinted and cultured in high-throughput arrays or tubes with either no changes or simple changes to MAGIC matrix composition, for example including collagen or excluding Matrigel. By a variety of mechanical and functional metrics, MAGIC matrices during cell culture at 37 °C are indistinguishable from pure Matrigel. For example, budding in salivary gland organoids is driven by strong cell-matrix interactions and weak cell-cell interactions[96,97]; these results imply that cell-matrix interactions were not disrupted by decreased Matrigel concentration or the presence of microgels. Overall, the broad spectrum of tissue types successfully produced using MAGIC matrix bioprinting highlights the utility of this material platform.

Combined, these technologies have important implications for the application of organoids in high-throughput biology, drug screens, and personalized medicine. To demonstrate the potential of this approach in high-throughput biology we leveraged scripting and automation to generate organoid arrays that underwent more rapid and more uniform morphogenesis than previously described methods. These arrays were amenable to both live and fixed imaging. Furthermore, these organoids could potentially be collected for dissociation, sorting, and sequencing. By controlling the initial conditions of tissue growth and eliminating extrinsic sources of heterogeneity, we demonstrated dramatic improvements in assay statistical power. We decreased the number of observations required to identify a statistically significant phenotype by an order of magnitude compared to traditional culture. Furthermore, as the number of observations increased, organoid arrays provided assay sensitivities many of orders of magnitude better than manual seeding. Therefore, this platform simultaneously requires fewer organoids and improves statistical power, presenting opportunities to work with rare cell types or primary patient biopsies for drug screens. Removing extrinsic heterogeneity also lays important groundwork for assays with complex readouts, long culture times, and poorly understood phenotypes, such as those involving human stem cell-derived organoids.

Finally, we present progress toward future construction of more complex and in vivo-like 3D microphysiological systems by perfusing bioprinted organoid tubes. The regularity and scalability of these models could be combined with established high-throughput pipelines for screening drugs or gene therapies using organ-on-chip platforms, but without the drawbacks of artificial interfaces and geometries. Ultimately, MAGIC matrix bioprinting combines multiple advances to take a large and meaningful step toward addressing the need for more complex and reproducible in vitro models of living tissues.

Materials and Methods

Materials and methods are provided in the supplement.

Data and Code Availability

All source data will be made available upon peer-reviewed publication. Custom MATLAB, R, and Image J Macro (IJM) scripts will be publicly made available through GitHub upon peer-reviewed publication or can be provided upon request.

Acknowledgements

We thank the members of the Gartner Lab, Klein Lab, and CZ Biohub Bioengineering Group for their valuable suggestions. We thank Sandra Montes-Olivas for guidance in the use of her MATLAB crypt counting software. We thank Dr. Kevin Healy for providing rheological equipment. This work was funded by the Chan Zuckerberg Investigator Program to Z.J.G., the UCSF Center for Cellular Construction (DBI-1548297), a CBCRP IDEA award, and the NIDDK (R01DK126376). A.J.G. was supported by a Chan Zuckerberg Biohub Collaborative Postdoctoral Fellowship. V.S. was supported by the Zena Werb Memorial Fellowship through the Helen Diller Family Cancer Center at UCSF. FACS was performed on a BD Aria 3, supported in part by HDFCCC Laboratory for Cell Analysis Shared Resource Facility through a grant from NIH (P30CA082103).

Author Contributions

A.J.G. and Z.J.G. conceptualized the embedded bioprinting material design and application. A.J.G., M.W.L.K., H.K., P.L., R.G.S., and Z.J.G. conceptualized the bioprinter instrumentation. A.J.G. performed materials synthesis and characterization. M.W.L.K., P.L., and R.G.S. designed and built the bioprinter hardware and wrote the software. A.J.G., V.S., S.V., K.M.H, and N.G. performed primary cell isolation, culture, microscopy, immunofluorescence, and organoid experiments. A.J.G., M.W.L.K., and H.K. performed experiments to identify optimal bioprinting parameters. M.W.L.K. wrote custom scripts for bioprinting organoid arrays. A.J.G., V.S., and M.B. wrote custom scripts for microscopy and statistical analysis. K.P., C.M., and S.K. consulted on and provided experimental assistance with material characterization. V.S., S.V., K.M.H., N.G., J.M.R., T.J.N., and O.K. consulted on and provided experimental assistance with organoid isolation, characterization, and application. A.J.G. and Z.J.G. wrote the manuscript, with review and feedback from all other authors.

Declaration of Interest

A.J.G., R.G.S., and Z.J.G. are co-inventors on a patent regarding the design and application of the embedded bioprinting material and piezoelectric printhead (U.S. Provisional Patent Application No. 63/605,710). Z.J.G. is an equity holder in Scribe biosciences, Provenance Bio, and Serotiny.

Extended Data Figure 1. MAGIC matrices are tunable embedded printing and cell culture biomaterials. A. Storage and loss modulus of (left) 0.5 wt% and (right) 1 wt% alginate microgel (AMG) slurry and Matrigel as a function of temperature. **B.** Storage and loss moduli of MAGIC matrix formulations at 37 °C using (left) 0.5 wt% AMGs and (right) 1 wt% AMGs at 1 Hz and 1% strain. Data shown are mean ± SD from n = 3 independent microgel preparations. * = $p < 0.05$ for both storage and loss modulus of all MAGIC matrix formulations using 1 wt% AMGs compared to pure Matrigel as determined by one-way ANOVA with Tukey's multiple comparisons. **C.** Oscillatory amplitude sweeps at 4 °C for various MAGIC matrix compositions show yielding behavior indicated by G' and G'' cross-over. Data shown are representative of n = 3 independent microgel preparations. **D.** Unidirectional shear rate measurements at 4 °C fit to a Herschel-Bulkley power law model. **E.** MAGIC matrix yield stress values calculated using Herschel-Bulkley fits in (D). Data shown are mean ± SD of n = 3 independent microgel preparations. **F.** Reversible yield-stress test wherein applied strain is alternated between 1% and 100% for a variety of MAGIC matrix formulations at 4 °C. Gray bars indicate areas of 100% strain. Cross-over and recovery of G' and G'' indicates reversible viscoelastic behavior. For **C**, **D**, and **F**, data are representative of *n* = 3 independent microgel preparations.

Extended Data Figure 2. MAGIC matrices exhibit composition-dependent plasticity and stress relaxation. A. Representative data illustrating different mechanical modes of a creep test meant to simulate tissue expansion with constant force. **B, C.** Creep test for 10 Pa applied constant shear stress (gray bar) for different MAGIC matrix formulations measuring material strain rate compared to pure Matrigel. **D–F.** Relaxation modulus measured during creep experiments shows corresponding differences in matrix stress relaxation. In general, response to applied stress is a strong function of alginate wt%, but not faction of Matrigel.

Extended Data Figure 3. MAGIC matrix composition impacts organoid morphogenetic phenotype. A. Representative images of mouse intestinal organoids at 5 days after manually seeding into Matrigel and MAGIC matrices of varying alginate microgel wt% and packing density (represented as added volume ratio of Matrigel:alginate microgel). MAGIC matrix compositions are represented as added volume ratio of Matrigel:alginate microgel. Scale bars = 200 µm. **B.** Quantification of organoid crypt width (top) and crypt length (bottom) as a function of matrix composition. **C.** Representative images of organoids grown in Matrigel diluted at various volume ratios with mouse intestinal organoid growth medium. Scale bars = 200 µm.

Extended Data Figure 4. Alginate microgels are roughly cell-sized. A. Cartoon workflow for preparation of alginate microgel slurry. **B.** Brightfield image of microgel slurry after synthesis, with nearly transparent microgels. Scale bar = 200 µm. **C.** Representative images outlining workflow for quantifying microgel size. The polyanionic alginate backbone was positively stained with DAPI and segmented in Fiji to calculate particle diameter. **D.** Distribution of alginate microgel sizes fit to a Gaussian distribution. Data shown are mean ± SD from *n* = 3 separate images from 3 separate fields of view for each alginate wt%.

Extended Data Figure 5. MAGIC matrices facilitate live and fixed imaging and promote canonical self-organization of various organoid types. A. Cartoon illustrating differences in organoid outgrowth and phenotype as a function of seeding technique. Traditional mechanical dissociation leads to a heterogeneous distribution of cell states, structures, and microenvironments. Dense cell slurry bioinks promote normalization of these factors to reduce extrinsic inter-organoid heterogeneity. **B.** Brightfield and fluorescent live images of mouse intestinal organoid arrays 2 days after bioprinting expressing either mTomato or *Lgr5*-localized GFP. GFP signal localizes to the base of the crypts, where *Lgr5*+ stem cells should reside. Scale bars = 500 µm. **C.** 3D renderings of fixed bioprinted intestinal organoid cysts (top) and tubes (bottom) showing positive signal for stem (Lgr5) and Paneth cell (lysozyme) by immunofluorescence. Crypts protrude in all directions, highlighting fully 3D morphogenesis in MAGIC matrices. **D.** Bioprinted intestinal organoids are positive for enteroendocrine cells (chromogranin-A). Scale bar = 100 µm. **E.** Live imaging of bioprinted salivary gland organoid arrays expressing mTomato. Scale bar = 1 mm. **F.** Immunofluorescence of fixed bioprinted salivary gland organoids showing presence of both basal (keratin 14) and ductal (keratin 8) cells. Scale bar = 100 µm.

Extended Data Figure 6. Bioprinted hiPSC-derived cortical brain organoids exhibit matrix-dependent phenotypes and rosette organization. A. hiPSC-derived cortical organoids from three different donors (methods) were bioprinted into arrays using alginate microgel support baths. Scale bar = 1 mm. **B.** Cortical organoids bioprinted in MAGIC matrices show sprouting (arrow) and neuroepithelial budding (arrowheads). Scale bars = 1 mm (left) and 500 µm (right). **C, D.** 20 µm maximum intensity projections of bioprinted cortical organoids stained for (C) cortical identity and (D) neuronal differentiation. Scale bars = 50 µm.

Extended Data Figure 7. Bioprinted TNBC patient-derived organoid arrays are efficiently transfected. A. Live images of bioprinted TNBC organoid arrays transfected using Lipofectamine RNAiMAX and a Cy3-conjugated, single-stranded non-coding small RNA (36mer) at various concentrations and transfection times. Scale bars = 500 µm.

Supplementary Movie 1. Dense cell slurry bioinks printed into pure Matrigel at 4 °C do not retain their printed shape.

Supplementary Movie 2. Example of high-throughput organoid array generation using MAGIC matrix bioprinting. Video is displayed at 8x real-time.

Supplementary Movie 3. MAGIC matrix bioprinting of HUVEC vascular cords.

Supplementary Movie 4. MAGIC matrix bioprinting of a mouse intestinal organoid tube.

Supplementary Movie 5. Cyclic 3D pressurization of a perfused intestinal organoid tube. Tube diameter increases and decreases upon application and removal of pressure, indicating the tissue is experiencing strain.

References

1. Dekkers, J. F. *et al.* A functional CFTR assay using primary cystic fibrosis intestinal organoids. *Nat Med* **19**, 939–945 (2013).

2. Clevers, H. Modeling Development and Disease with Organoids. *Cell* **165**, 1586–1597 (2016).

3. Koike, H. *et al.* Modelling human hepato-biliary-pancreatic organogenesis from the foregut–midgut boundary. *Nature* **574**, 112–116 (2019).

4. Driehuis, E., Kretzschmar, K. & Clevers, H. Establishment of patient-derived cancer organoids for drug-screening applications. *Nat Protoc* **15**, 3380–3409 (2020).

5. Jiang, S. *et al.* An Automated Organoid Platform with Inter-organoid Homogeneity and Inter-patient Heterogeneity. *Cell Reports Medicine* **1**, 100161 (2020).

6. Hofer, M. & Lutolf, M. P. Engineering organoids. *Nat Rev Mater* **6**, 402–420 (2021).

7. Wolf, K. J., Weiss, J. D., Uzel, S. G. M., Skylar-Scott, M. A. & Lewis, J. A. Biomanufacturing human tissues via organ building blocks. *Cell Stem Cell* **29**, 667–677 (2022).

8. Viragova, S. *et al.* Inverse agonists of retinoic acid receptor/retinoid X receptor signaling as lineage-specific antitumor agents against human adenoid cystic carcinoma. *JNCI: J. Natl. Cancer Inst.* **115**, 838–852 (2023).

9. Sato, T. *et al.* Single Lgr5 stem cells build crypt-villus structures in vitro without a mesenchymal niche. *Nature* **459**, 262–265 (2009).

10. Gjorevski, N. *et al.* Designer matrices for intestinal stem cell and organoid culture. *Nature* **539**, 560–564 (2016).

11. Broguiere, N. *et al.* Growth of Epithelial Organoids in a Defined Hydrogel. *Adv. Mater.* **30**, e1801621 (2018).

12. Aisenbrey, E. A. & Murphy, W. L. Synthetic alternatives to Matrigel. *Nat Rev Mater* 1–13 (2020) doi:10.1038/s41578-020-0199-8.

13. Rezakhani, S., Gjorevski, N. & Lutolf, M. P. Extracellular matrix requirements for gastrointestinal organoid cultures. *Biomaterials* **276**, 121020 (2021).

14. Hunt, D. R. *et al.* Engineered Matrices Enable the Culture of Human Patient-Derived Intestinal Organoids. *Adv Sci* **8**, 2004705 (2021).

15. Brassard, J. A. & Lutolf, M. P. Engineering Stem Cell Self-organization to Build Better Organoids. *Cell Stem Cell* **24**, 860–876 (2019).

16. Beck, L. E. *et al.* Systematically quantifying morphological features reveals constraints on organoid phenotypes. *Cell Syst* **13**, 547-560.e3 (2022).

17. Lukonin, I., Zinner, M. & Liberali, P. Organoids in image-based phenotypic chemical screens. *Exp. Mol. Med.* **53**, 1495–1502 (2021).

18. Tallapragada, N. P. *et al.* Inflation-collapse dynamics drive patterning and morphogenesis in intestinal organoids. *Cell Stem Cell* **28**, 1516-1532.e14 (2021).

19. Serra, D. *et al.* Self-organization and symmetry breaking in intestinal organoid development. *Nature* **569**, 66–72 (2019).

20. Bues, J. *et al.* Deterministic scRNA-seq captures variation in intestinal crypt and organoid composition. *Nat Methods* 1–8 (2022) doi:10.1038/s41592-021-01391-1.

21. Jensen, K. B. & Little, M. H. Organoids are not organs: Sources of variation and misinformation in organoid biology. *Stem Cell Rep.* **18**, 1255–1270 (2023).

22. Srivastava, V. *et al.* Configurational entropy is an intrinsic driver of tissue structural heterogeneity. *bioRxiv* 2023.07.01.546933 (2023) doi:10.1101/2023.07.01.546933.

23. Sockell, A. *et al.* A microwell platform for high-throughput longitudinal phenotyping and selective retrieval of organoids. *Cell Syst.* **14**, 764-776.e6 (2023).

24. Lin, F. *et al.* Mechanically enhanced biogenesis of gut spheroids with instability-driven morphomechanics. *Nat. Commun.* **14**, 6016 (2023).

25. Brandenberg, N. *et al.* High-throughput automated organoid culture via stem-cell aggregation in microcavity arrays. *Nat Biomed Eng* **4**, 863–874 (2020).

26. Huh, D. *et al.* Reconstituting Organ-Level Lung Functions on a Chip. *Science* **328**, 1662–1668 (2010).

27. Jalili-Firoozinezhad, S. *et al.* A complex human gut microbiome cultured in an anaerobic intestine-on-a-chip. *Nat Biomed Eng* **3**, 520–531 (2019).

28. Nikolaev, M. *et al.* Bioengineering microfluidic organoids-on-a-chip. (2020) doi:10.21203/rs.3.pex-903/v1.

29. Nikolaev, M. *et al.* Homeostatic mini-intestines through scaffold-guided organoid morphogenesis. *Nature* **585**, 574–578 (2020).

30. Madden, L. R. *et al.* Bioprinted 3D Primary Human Intestinal Tissues Model Aspects of Native Physiology and ADME/Tox Functions. *Iscience* **2**, 156–167 (2018).

31. Hinton, T. J. *et al.* Three-dimensional printing of complex biological structures by freeform reversible embedding of suspended hydrogels. *Sci Adv* **1**, e1500758 (2015).

32. Bakht, S. M. *et al.* 3D Bioprinting of Miniaturized Tissues Embedded in Self-Assembled Nanoparticle-Based Fibrillar Platforms. *Adv. Funct. Mater.* **31**, (2021).

33. Daly, A. C., Davidson, M. D. & Burdick, J. A. 3D bioprinting of high cell-density heterogeneous tissue models through spheroid fusion within self-healing hydrogels. *Nat Commun* **12**, 753 (2021).

34. Lee, Y. B. *et al.* Induction of Four-Dimensional Spatiotemporal Geometric Transformations in High Cell Density Tissues via Shape-Changing Hydrogels. *Adv. Funct. Mater.* **31**, 2010104 (2021).

35. Lawlor, K. T. *et al.* Cellular extrusion bioprinting improves kidney organoid reproducibility and conformation. *Nat Mater* **20**, 260–271 (2021).

36. McLoughlin, S. T., McKenna, A. R. & Fisher, J. P. 4d Bioprinting via Molecular Network Contraction for Membranous Tissue Fabrication. *Adv. Healthc. Mater.* e2300642 (2023) doi:10.1002/adhm.202300642.

37. Song, M. J. *et al.* Bioprinted 3D outer retina barrier uncovers RPE-dependent choroidal phenotype in advanced macular degeneration. *Nat Methods* **20**, 149–161 (2023).

38. Urciuolo, A. *et al.* Hydrogel-in-hydrogel live bioprinting for guidance and control of organoids and organotypic cultures. *Nat Commun* **14**, 3128 (2023).

39. Daly, A. C., Prendergast, M. E., Hughes, A. J. & Burdick, J. A. Bioprinting for the Biologist. *Cell* **184**, 18–32 (2021).

40. Ho, D. L. L. *et al.* Large-Scale Production of Wholly Cellular Bioinks via the Optimization of Human Induced Pluripotent Stem Cell Aggregate Culture in Automated Bioreactors. *Adv Healthc Mater* 2201138 (2022) doi:10.1002/adhm.202201138.

41. Todhunter, M. E. *et al.* Programmed synthesis of three-dimensional tissues. *Nat Methods* **12**, 975–981 (2015).

42. Gjorevski, N. *et al.* Tissue geometry drives deterministic organoid patterning. *Science* **375**, eaaw9021 (2022).

43. Prahl, L. S., Porter, C. M., Liu, J., Viola, J. M. & Hughes, A. J. Independent control over cell patterning and adhesion on hydrogel substrates for tissue interface mechanobiology. *iScience* **26**, 106657 (2023).

44. Porter, C. M., Qian, G. C., Grindel, S. H. & Hughes, A. J. Highly parallel production of designer organoids by mosaic patterning of progenitors. *Cell Syst.* **15**, 649-661.e9 (2024).

45. Hughes, A. J. *et al.* Engineered Tissue Folding by Mechanical Compaction of the Mesenchyme. *Dev Cell* **44**, 165-178.e6 (2018).

46. Cabral, K. A. *et al.* Simple, Affordable, and Modular Patterning of Cells using DNA. *J Vis Exp* (2021) doi:10.3791/61937.

47. Cabral, K. A. *et al.* Programming the Self-Organization of Endothelial Cells into Perfusable Microvasculature. *Tissue Eng Pt A* **29**, 80–92 (2023).

48. Brassard, J. A., Nikolaev, M., Hübscher, T., Hofer, M. & Lutolf, M. P. Recapitulating macro-scale tissue self-organization through organoid bioprinting. *Nat Mater* **20**, 22–29 (2021).

49. Bhattacharjee, T. *et al.* Writing in the granular gel medium. *Sci Adv* **1**, e1500655 (2015).

50. Morley, C. D. *et al.* Quantitative characterization of 3D bioprinted structural elements under cell generated forces. *Nature Communications* 1–9 (2019) doi:10.1038/s41467-019-10919-1.

51. O'Bryan, C. S., Kabb, C. P., Sumerlin, B. S. & Angelini, T. E. Jammed Polyelectrolyte Microgels for 3D Cell Culture Applications: Rheological Behavior with Added Salts. *Acs Appl Bio Mater* **2**, 1509–1517 (2019).

52. Morley, C. D., Tordoff, J., O'Bryan, C. S., Weiss, R. & Angelini, T. E. 3D aggregation of cells in packed microgel media. *Soft Matter* **16**, 6572–6581 (2020).

53. Reynolds, D. S. *et al.* Microporogen-Structured Collagen Matrices for Embedded Bioprinting of Tumor Models for Immuno-Oncology. *Adv. Mater.* e2210748 (2023) doi:10.1002/adma.202210748.

54. Brunel, L. G. *et al.* Embedded 3D Bioprinting of Collagen Inks into Microgel Baths to Control Hydrogel Microstructure and Cell Spreading. *Adv. Healthc. Mater.* e2303325 (2024) doi:10.1002/adhm.202303325.

55. Chaudhuri, O., Cooper-White, J., Janmey, P. A., Mooney, D. J. & Shenoy, V. B. Effects of extracellular matrix viscoelasticity on cellular behaviour. *Nature* **584**, 535–546 (2020).

56. Yui, S. *et al.* YAP/TAZ-Dependent Reprogramming of Colonic Epithelium Links ECM Remodeling to Tissue Regeneration. *Cell Stem Cell* **22**, 35-49.e7 (2018).

57. Mandal, K. *et al.* Soft Hyaluronic Gels Promote Cell Spreading, Stress Fibers, Focal Adhesion, and Membrane Tension by Phosphoinositide Signaling, Not Traction Force. *ACS Nano* **13**, 203–214 (2019).

58. Kobayashi, S. *et al.* Collagen type I-mediated mechanotransduction controls epithelial cell fate conversion during intestinal inflammation. *Inflamm. Regen.* **42**, 49 (2022).

59. Pérez-González, C. *et al.* Mechanical compartmentalization of the intestinal organoid enables crypt folding and collective cell migration. *Nat Cell Biol* **23**, 745–757 (2021).

60. Lei, I. M. *et al.* Soft Hydrogel Shapeability via Supportive Bath Matching in Embedded 3D Printing. *Adv. Mater. Technol.* **8**, (2023).

61. Tournier, P. *et al.* Clickable Dynamic Bioinks Enable Post-Printing Modifications of Construct Composition and Mechanical Properties Controlled over Time and Space. *Adv. Sci.* e2300055 (2023) doi:10.1002/advs.202300055.

62. Chaudhuri, O. *et al.* Hydrogels with tunable stress relaxation regulate stem cell fate and activity. *Nat Mater* **15**, 326–334 (2016).

63. Elosegui-Artola, A. *et al.* Matrix viscoelasticity controls spatiotemporal tissue organization. *Nat. Mater.* **22**, 117–127 (2023).

64. Nerger, B. A. *et al.* 3D Hydrogel Encapsulation Regulates Nephrogenesis in Kidney Organoids. *Adv. Mater.* e2308325 (2024) doi:10.1002/adma.202308325.

65. Nam, S., Lee, J., Brownfield, D. G. & Chaudhuri, O. Viscoplasticity Enables Mechanical Remodeling of Matrix by Cells. *Biophys. J.* **111**, 2296–2308 (2016).

66. Tee, S.-Y., Bausch, A. R. & Janmey, P. A. The mechanical cell. *Curr. Biol.* **19**, R745–R748 (2009).

67. Yang, Q. *et al.* Cell fate coordinates mechano-osmotic forces in intestinal crypt formation. *Nat Cell Biol* 1–12 (2021) doi:10.1038/s41556-021-00700-2.

68. Groll, J. *et al.* A definition of bioinks and their distinction from biomaterial inks. 1–6 (2018) doi:10.1088/1758-5090/aaec52.

69. Sun, W. *et al.* The bioprinting roadmap. *Biofabrication* **12**, 022002 (2020).

70. Morley, C. D. *et al.* Spatiotemporal T cell dynamics in a 3D bioprinted immunotherapy model. *Bioprinting* e00231 (2022) doi:10.1016/j.bprint.2022.e00231.

71. Zhu, J. & Cai, L.-H. All-Aqueous Printing of Viscoelastic Droplets in Yield-Stress Fluids. *Acta Biomater* (2022) doi:10.1016/j.actbio.2022.09.031.

72. Becker, M., Gurian, M., Schot, M. & Leijten, J. Aqueous Two-Phase Enabled Low Viscosity 3D (LoV3D) Bioprinting of Living Matter. *Adv. Sci.* **10**, 2204609 (2023).

73. Hijnen, N. & Clegg, P. S. Colloidal Aggregation in Mixtures of Partially Miscible Liquids by Shear-Induced Capillary Bridges. *Langmuir* **30**, 5763–5770 (2014).

74. Vasilyev, O. A., Labbé-Laurent, M., Dietrich, S. & Kondrat, S. Bridging transitions and capillary forces for colloids in a slit. *J. Chem. Phys.* **153**, 014901 (2020).

75. Navis, A. & Bagnat, M. Developing pressures: fluid forces driving morphogenesis. *Curr. Opin. Genet. Dev.* **32**, 24–30 (2015).

76. Raghavan, S. *et al.* Decoupling diffusional from dimensional control of signaling in 3D culture reveals a role for myosin in tubulogenesis. *J Cell Sci* **123**, 2877–2883 (2010).

77. Palikuqi, B. *et al.* Adaptable haemodynamic endothelial cells for organogenesis and tumorigenesis. *Nature* **585**, 426–432 (2020).

78. Kajtez, J. *et al.* Embedded 3D Printing in Self-Healing Annealable Composites for Precise Patterning of Functionally Mature Human Neural Constructs. *Adv Sci* 2201392 (2022) doi:10.1002/advs.202201392.

79. Fang, Y. *et al.* Expanding Embedded 3D Bioprinting Capability for Engineering Complex Organs with Freeform Vascular Networks. *Adv. Mater.* **35**, e2205082 (2023).

80. Franca, C. M. *et al.* High-Throughput Bioprinting of Geometrically-Controlled Pre-Vascularized Injectable Microgels for Accelerated Tissue Regeneration. *Adv. Healthc. Mater.* e2202840 (2023) doi:10.1002/adhm.202202840.

81. Xiong, F. *et al.* Specified Neural Progenitors Sort to Form Sharp Domains after Noisy Shh Signaling. *Cell* **153**, 550–561 (2013).

82. Huycke, T. R. *et al.* Patterning and folding of intestinal villi by active mesenchymal dewetting. *Cell* (2024) doi:10.1016/j.cell.2024.04.039.

83. Cerchiari, A. E. *et al.* A strategy for tissue self-organization that is robust to cellular heterogeneity and plasticity. *Proc National Acad Sci* **112**, 2287–2292 (2015).

84. Popova, G. *et al.* Human microglia states are conserved across experimental models and regulate neural stem cell responses in chimeric organoids. *Cell Stem Cell* **28**, 2153-2166.e6 (2021).

85. Shin, D. *et al.* Thalamocortical organoids enable in vitro modeling of 22q11.2 microdeletion associated with neuropsychiatric disorders. *Cell Stem Cell* **31**, 421-432.e8 (2024).

86. Lancaster, M. A. *et al.* Cerebral organoids model human brain development and microcephaly. *Nature* **501**, 373–379 (2013).

87. Lancaster, M. A. & Knoblich, J. A. Generation of cerebral organoids from human pluripotent stem cells. *Nat. Protoc.* **9**, 2329–2340 (2014).

88. Andersen, J. *et al.* Generation of Functional Human 3D Cortico-Motor Assembloids. *Cell* **183**, 1913-1929.e26 (2020).

89. Reyes, E. A. *et al.* Epithelial TNF controls cell differentiation and CFTR activity to maintain intestinal mucin homeostasis. *J. Clin. Investig.* **133**, e163591 (2023).

90. Montes-Olivas, S. *et al.* In-silico and in-vitro morphometric analysis of intestinal organoids. *PLOS Comput. Biol.* **19**, e1011386 (2023).

91. McKinley, K. L. *et al.* Cellular aspect ratio and cell division mechanics underlie the patterning of cell progeny in diverse mammalian epithelia. *eLife* **7**, e36739 (2018).

92. Castillo-Azofeifa, D. *et al.* Atoh1+ secretory progenitors possess renewal capacity independent of Lgr5+ cells during colonic regeneration. *Embo J* **38**, (2019).

93. Muir, V. G. *et al.* Influence of Microgel and Interstitial Matrix Compositions on Granular Hydrogel Composite Properties. *Adv Sci* 2206117 (2023) doi:10.1002/advs.202206117.

94. Morley, C. D., Ding, E. A., Carvalho, E. M. & Kumar, S. A Balance Between Inter- and Intra- Microgel Mechanics Governs Stem Cell Viability in Injectable Dynamic Granular Hydrogels. *Adv. Mater.* e2304212 (2023) doi:10.1002/adma.202304212.

95. Carvalho, E. M. & Kumar, S. Lose the stress: Viscoelastic materials for cell engineering. *Acta Biomater.* **163**, 146–157 (2023).

96. Wang, S., Matsumoto, K., Lish, S. R., Cartagena-Rivera, A. X. & Yamada, K. M. Budding epithelial morphogenesis driven by cell-matrix versus cell-cell adhesion. *Cell* (2021) doi:10.1016/j.cell.2021.05.015.

97. Cazares, O., Haque, A. S. & Klein, O. D. Salivary gland: A budding genius. *Dev Cell* **56**, 2271–2272 (2021).

A
Manual Organoid Seeding
variable initial conditions
• tissue size
• tissue composition
• media access
• xyz position
self-
organization
+treatment
heterogeneous phenotypes
MAGIC Matrix Bioprinting
piezoelectric printhead
ink plate
organoid slurry bioink
array
bioprinting
tube
bioprinting
print plate
organoid seeds
self-
organization
cyst formation
+treatment
homogeneous phenotypes
organoid tubes
self-
organization
lumenization
+perfusion
−cell debris; +media, drugs
3D microphysiological system
B
1
MAGIC matrix
printing
at 4 °C
soft alginate
microgels
basement
membrane
print plate
morphogenesis
at 37 °C
organoid array
microscope aligned to print
printhead z-stage
chilled bioink
plate
xy-stage
2
piezoelectric printhead
fluidics port
piezoelectric
actuator
fluid-filled cavity
PEEK diaphragm
125 µm ID
micropipette
cell slurry bioink
aspiration (↑)
or extrusion (↓)
C
viscous interstitial
ECM (Matrigel)
granular microgel
support (alginate)
+
mix @ 4 °C
Matrigel Alginate
Matrigel-Alginate Granular-Interstitial Composite
(MAGIC) Matrix
D
Z
X
Y
Printhead
z = dish bottom
z = printhead
height
Matrigel at 4 °C
MAGIC Matrix at 4 °C
E
4 °C
37 °C
printhead enters
MAGIC matrix
organoid bioink
is extruded
morphogenesis
Printhead

Printing conditions: 4 °C
Culture conditions: 37 °C
Morphogenesis: 37 °C
A
MAGIC Matrix:
1:2 1:1 2:1
● G'
○ G''
4 °C
Shear Modulus (Pa)
Shear Stress (Pa)
B
4 °C
Yield stress (Pa):
1.9 ± 0.6
0.7 ± 0.1
0.2 ± 0.03
**
Calculated Yield Stress (Pa)
1:2
1:1
2:1
C
37 °C
● G'
○ G''
**
ns
Modulus at 37 °C (Pa)
1 wt%
0.5 wt%
Matrigel
D
37 °C
MAGIC Matrix:
1 wt%
0.5 wt%
Matrigel
10 Pa Applied Stress
Relaxation Modulus (Pa)
Time (s)
E
Matrigel
0.5 wt%; 1:1
1 wt%; 1:1
0.5 wt%; 1:2
F
****
ns
Crypt Width (µm)
Matrigel
0.5 wt%
1 wt%
G
****
ns
Crypt Length (µm)
Matrigel
1:1
1:2

A
tail-breaking script
1 extrusion step
2 move printhead up in z
3 rapid negative pressure & xy-displacement
4 active mechanics & compaction
B
GFP
without
with
y
x
z
x
C
Day 0
compaction
Day 3
Piezo Extrusion Step Size (µm)
0.01
0.05
0.1
0.2
D
Organoid Area (µm²)
5×10⁴
4×10⁴
3×10⁴
2×10⁴
1×10⁴
0
Day 0
Day 3
0.01
0.05
0.10
0.20
Extrusion Step (µm)
E
Organoid Circularity
1.0
0.8
0.6
0.4
0.2
0.0
Day 0
Day 3
0.01
0.05
0.10
0.20
Extrusion Step (µm)
F
media
i
ii
iii
cover glass
(i) 250 µm
(ii) 500 µm
(iii) 1000 µm
Day 0
Day 7
G
(ii) 500 µm array
Day 6
Day 11
H
media
i
ii
iii
cover glass
(i) 500 µm
(ii) 1000 µm
(iii) 1500 µm
mTomato
I
Organoid Area (µm²)
2.0×10⁵
1.5×10⁵
1.0×10⁵
5.0×10⁴
0.0
Day 5
Day 7
ns
****
****
500
1000
1500
Height from Bottom (µm)

A
Day 0
Tube Diameter (μm)
300
200
100
0
0.0
0.2
0.4
0.6
0.8
Extrusion Speed (μm/s)
Stage Speed
200 μm/s
400 μm/s
Day 3
Tube Diameter (μm)
Extrusion Speed (μm/s)
B
Day 0
Day 7
mCherry
C
Day 0
Day 3
D
Z
X
Y
manual perfusion
cleared lumen
no flow
+ flow
d
cell debris
cleared lumen
no flow
+flow
E
Diameter (μm)
350
325
300
275
250
Strain (%)
40
30
20
10
0
Time (s)
0
20
40
60
80
100
120

A
Mouse Small Intestine
morphogenesis
DAPI
ECAD LGR5
ECAD
DAPI
LYZ
B
morphogenesis
ECAD
DAPI
ECAD
LGR5
ECAD
LYZ
C
Human Mammary
sorting
LEP MEP
+1 day
1:1 LEP:MEP
2:1 LEP:MEP
D
1:1
2:1
All MEP
1:1 LEP:MEP
2:1 LEP:MEP
1:1 MEP:MEP
Boundary Fraction LEP
1.0
0.8
0.6
0.4
0.2
0.0
E
Human Cortical Brain
Manual Seeding
growth
Day 1
Day 15
96 well
ULA
96 well
ULA
Organoid Seed Bioprinting
growth
Day 1
Day 5
Day 9
Day 14
F
FOXG1
DLX2
DAPI
PAX6
EOMES
CTIP2
DAPI
Control
Printed
ns
ns
% positive
80
60
40
20
0
FOXG1
DLX2
Control
Printed
**
ns
ns
% positive
80
60
40
20
0
PAX6
EOMES
CTIP2

A
Matrigel
Lenti-GFP
MAGIC matrix
Lenti-GFP
B
Fraction Infected Organoids
1.2
1.0
0.8
0.6
0.4
0.2
0.0
Matrigel
MAGIC matrix
ns
****
Suspension
Matrix
C
Lenti-GFP
Cy3
BF
D
morphogenesis
Day 0
Day 2
Day 5
Day 5
mTOMATO
E
Organoid Area (μm²)
10⁶
10⁵
10⁴
10³
10²
Day 0
Day 2
Day 5
Manual
Bioprinted
F
No. of Crypts per Organoid
10
8
6
4
2
0
Day 5
****
ns
Manual
Manual (MAGIC)
Bioprinted
G
Atoh1CreERT2;Rosa26tdTomato
Image
Seed + DAPT
4OHT
D0
D1
D2
D3
H
–DAPT
+DAPT
I
–DAPT
+DAPT
J
tdTomato+ Volume (μm³)
10⁸
10⁷
10⁶
10⁵
10⁴
10³
10²
****
****
+Treatment
–Treatment
Printed
Manual
K
P-value
0.6
0.4
0.2
0.0
p = 0.05
Printed
Manual
No. of Organoids Analyzed
0
10
20
30
40
50